



HAL
open science

Selenium mobility in a major Chalk aquifer (Lille metropolis, northern France): Contaminants cycles driven by geology, redox processes and pumping

Lise Cary, Angélie Portal, Gabriel Billon, Marc Parmentier, Véronique Alaimo, Aurélie Bouvet-Swialkowski, Philippe Négrel

► To cite this version:

Lise Cary, Angélie Portal, Gabriel Billon, Marc Parmentier, Véronique Alaimo, et al.. Selenium mobility in a major Chalk aquifer (Lille metropolis, northern France): Contaminants cycles driven by geology, redox processes and pumping. *Chemical Geology*, 2021, 583, pp.120465. 10.1016/j.chemgeo.2021.120465 . hal-03320820

HAL Id: hal-03320820

<https://brgm.hal.science/hal-03320820>

Submitted on 20 Aug 2021

HAL is a multi-disciplinary open access archive for the deposit and dissemination of scientific research documents, whether they are published or not. The documents may come from teaching and research institutions in France or abroad, or from public or private research centers.

L'archive ouverte pluridisciplinaire **HAL**, est destinée au dépôt et à la diffusion de documents scientifiques de niveau recherche, publiés ou non, émanant des établissements d'enseignement et de recherche français ou étrangers, des laboratoires publics ou privés.

1 **Selenium mobility in a major Chalk aquifer (Lille metropolis,**
2 **northern France): contaminants cycles driven by geology, redox**
3 **processes and pumping**

4 Lise Cary¹, Angélie Portal², Gabriel Billon³, Marc Parmentier¹, Véronique Alaimo³,
5 Aurélie Bouvet-Swialkowski⁴, Philippe Négrel²

6 ¹ BRGM, F-59810 Lesquin, France

7 ² BRGM, F-45060 Orléans, France

8 ³ LASIRE, Lille University, F-59655 Villeneuve d'Ascq

9 ⁴ Lille European Metropolis, F-59000, France

10 **Abstract**

11 Chalk groundwater in northern France presents selenium (Se) concentrations from <10 to 70 µg L⁻¹,
12 partly exceeding the latest European Framework Directive's drinking-water limit value of 20 µg L⁻¹.
13 Better to understand the heterogeneous dynamics of Se, we used a combination of geochemical,
14 isotopic and geophysical tools on a study site belonging to the Metropolis of Lille, France. This
15 approach provided a fine understanding of the Se fate in a dynamic redox system constrained by
16 geology, related redox processes and pumping, illustrating how local *versus* global controls affect the
17 Se cycling. A remarkable redox sequence controls element transfers in groundwater with a
18 progressive creation of reductive conditions. Highlighted by geophysical tools, a wide fracture corridor
19 in the Chalk formation disrupts the geological setting of this redox sequence. Under pumping, this
20 corridor allows the mixing of oxygenated groundwater with groundwater under reducing conditions.
21 The evolution of isotopic compositions of sulphate molecules confirms the global reduction trend of
22 sulphates, while pyrite oxidation occurs very locally, together with high Se concentrations. Pyrite is
23 expected to play a predominant role in Se mobility in the Chalk aquifer. Se and other redox sensitive
24 elements (Fe, Mn, N and S) undergo multiple redox cycles, resulting in a Se-rich redox front that
25 migrates downward over time within the water-level fluctuation zone of the porous Chalk. With the
26 decreasing trend of water levels caused by global changes, a Se stock could be immobilized in the
27 unsaturated zone, but nitrate content and redox conditions in the saturated zone will be major drivers
28 for Se mobility.

29
30 **1. Introduction**

31 Selenium (Se)—a non-metallic element of nutritional and toxicological importance—has been
32 intensively studied in terms of biological effects and environmental concern, notably because

33 of its Janus-faced properties (toxicity vs. antioxidant, mutagenic vs. anti-mutagenic) that are
34 highly dependent on its concentration and speciation (Brozmanová et al., 2010; Rayman,
35 2000; Vinceti et al., 2013). Se mobility, toxicity, bioavailability and bioaccumulation are linked
36 to its speciation, and are controlled by sorption and redox reactions (Sharma et al., 2014). Se
37 occurs in various oxidation states (VI, IV, 0, -II), as inorganic species and as organo-Se
38 complexes. The most common Se species within surface water, groundwater and soil are
39 selenate (Se(VI), SeO_4^{2-}) and selenite (Se(IV), SeO_3^{2-}) oxyanions that are highly soluble,
40 though Se(IV) adsorbs to solids more strongly at neutral pH (Neal and Sposito, 1989). SeO_4^{2-}
41 with the highest oxidation state can be chemically reduced to SeO_3 , which can be further
42 reduced to elemental Se(0) or selenomethionine (SeMet) that may then be volatilized as
43 dimethyl selenium (DMS_e). Selenium intake through drinking water occurs mainly in its
44 inorganic form that is generally more toxic than organic compounds, Se(VI) being the most
45 toxic species (Tugarova et al., 2013).

46 Excess Se levels in agricultural soil or within subsurface agricultural drainage- and
47 ground-waters have caused severe health problems in animals and humans, e.g. in the
48 United States (Ohlendorf and Santolo, 1994), China (Yang et al., 1983) or India (Bajaj et al.,
49 2011; Dhillon and Dhillon, 1991)... Se occurs naturally as a trace element in geologic
50 formations, mainly shale, e.g., (Kulp and Pratt, 2004; Mast et al., 2014; Parnell et al., 2016;
51 Stillings and Amacher, 2010; Tuttle et al., 2014), conglomerates (Dhillon and Dhillon, 2014),
52 coal (Liu et al., 2013) and sediments (Beisner et al., 2009; Cary et al., 2014; Masscheleyn et
53 al., 1991).

54 The general increase in water demand, and the change in amounts and periods of
55 natural recharge in the current times of global climate change, modify groundwater levels
56 and saturation conditions of Earth's critical zone and thereby the biogeochemical cycle of
57 chemicals like Se (Mitchell et al., 2012). The result is the risk of delivering water that does
58 not comply with drinking water standards. For the purpose of health control, the recent
59 version of the European Water Framework Directive WFD (2020/2184) has increased the Se
60 threshold value for human consumption to $20 \mu\text{g L}^{-1}$, compared to $10 \mu\text{g L}^{-1}$ in the initial WFD

61 (2000/60/EC). An increase up to $30 \mu\text{g L}^{-1}$ can be accepted if a natural origin of Se is shown,
62 although a reassessment of a safe upper limit of Se of $1 \mu\text{g L}^{-1}$ in drinking water is
63 recommended as toxic effects of Se species occur at low concentrations (Barron et al., 2009;
64 Vinceti et al., 2013).

65 Redox processes in groundwater are complex because they are linked to kinetics and
66 to a microbially activated network of reactions ; contaminant fate in redox-dynamic systems
67 thus needs specific studies (Borch et al., 2010). Selenium oxyanions can be microbially
68 reduced via dissimilatory reduction processes mainly to insoluble elemental Se(0) (Oremland
69 et al., 1989), which can be further reduced to selenide, Se(-II) (Fernández-Martínez and
70 Charlet, 2009; Herbel et al., 2003; Séby et al., 1997). Under reducing conditions, Se(0) and
71 Se(-II) become the dominant species (Zhang and Moore, 1996). Microorganisms can also
72 produce volatile Se-methyl forms and Se-II organic compounds (Chasteen and Bentley,
73 2003).

74 Bacterial respiration will transfer electrons from an energy source (organic matter or
75 minerals such as FeS_2), termed electron donor, to oxygenated species or electron acceptors
76 like dissolved dioxygen (O_2), nitrate (NO_3^-), or selenate Se(VI), Mn(IV), Fe(III), and sulphate
77 (SO_4^{2-}) (Bailey, 2016). In groundwater, the chemical reduction of SeO_4^{2-} to SeO_3^{2-} occurs after
78 reduction of O_2 and NO_3^- . Abiotic redox reactions also play an important role in Se cycling
79 (Breynaert et al., 2008). A variety of Fe(II)-bearing minerals can enhance abiotical Se(IV) or
80 Se(VI) reduction to Se(0), such as green rust, pyrite or mackinawite (Breynaert et al., 2008;
81 Kang et al., 2011; Schellenger and Larese-Casanova, 2013). However, little is known about
82 the Se oxidation. Under aerobic conditions, microbial oxidation promote both Se
83 volatilization, retention (Darcheville et al., 2008) and production of Se(VI) from Se(0) (Dowdle
84 and Oremland, 1998). The oxidation of Se-bearing pyrite by O_2 or NO_3^- releases Se(VI) into
85 groundwater (Stillings and Amacher, 2010). Finally, Se(IV) sorbe more than Se(VI) onto
86 organic matter, clay, iron oxides and iron sulphides (Coppin et al., 2009; Goldberg et al.,
87 2007).

88 Earlier, we studied the spatial disparities in Sr isotopic signatures, and Sr and Se
89 contents in the Chalk aquifer along the northern edge of the Paris Basin (France) to
90 successfully identify Se origins in the aquifer (Cary et al., 2014). The present study focuses
91 on the redox processes affecting Se dynamics in the same Chalk aquifer. Because the large-
92 scale evolution of surficial systems can be controlled by very localized biogeochemical
93 processes, we propose a multi-scale and interdisciplinary characterization, from bedrock to
94 aquifer. Geophysical imaging and solid analysis documented the spatial geological
95 heterogeneities. The processes affecting groundwater chemistry were assessed along with
96 monitoring of the wells, and the analysis of $\delta^{34}\text{S}$ and $\delta^{18}\text{O}$ of sulphate. This approach led to a
97 fine understanding of the Se cycle, constrained by the geology of the Chalk aquifer of
98 Northern France and by related redox processes as well as by pumping, illustrating how it is
99 controlled either by both local and global constraints.

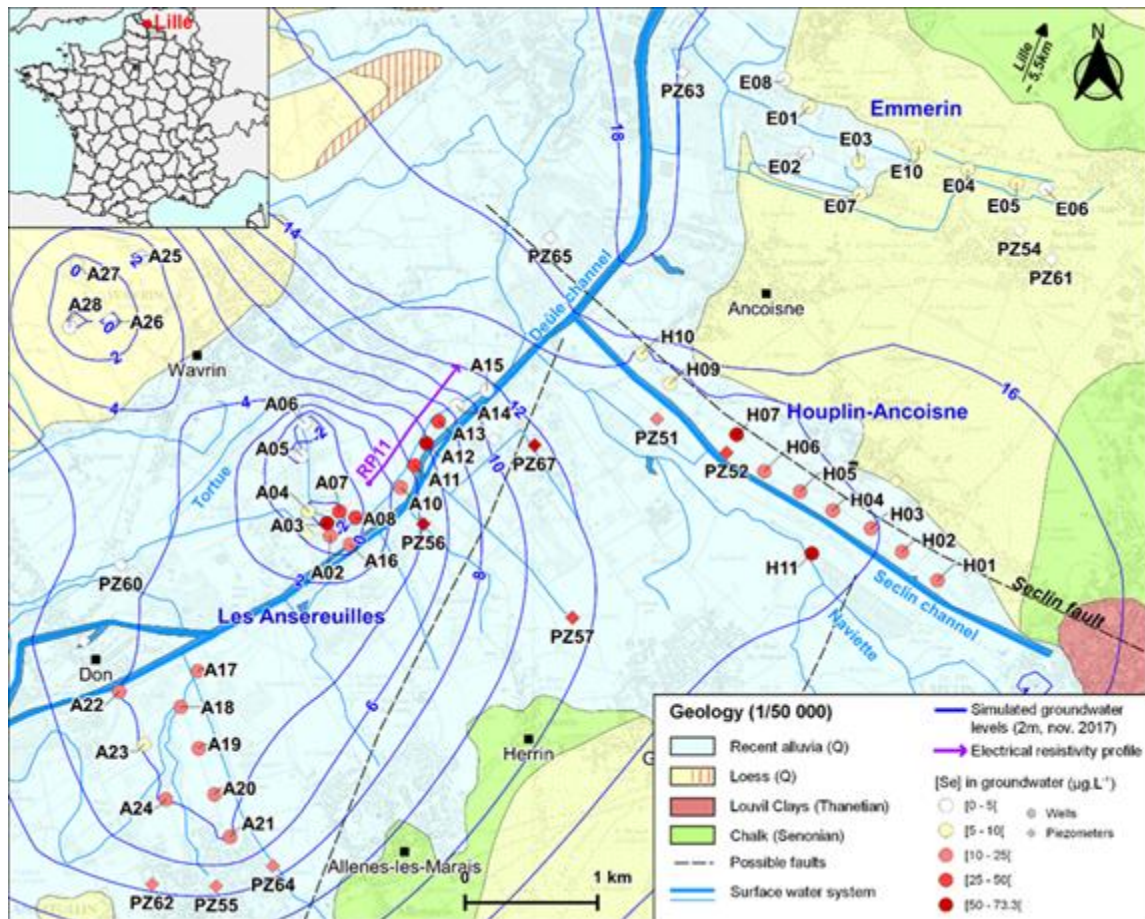
100 **2. Geological and hydrogeological context**

101 The north of France is part of the northern margin of the Paris Basin, one of the main
102 geological units of Western Europe. Local outcrops range from Late Cretaceous to the
103 Quaternary (*Figure Fig. 1*). The "Dièves" clayey marls of Early and Middle Turonian age are
104 up to 70 m thick. The overlying Senonian-Turonian white Chalk is up to 70 m thick. Above,
105 local Tertiary deposits are composed of Louvil clays (Early Thanetian; 9-12 m thick), the
106 Ostricourt sands (Late Thanetian; >30 m thick locally) and the Orchies or Flandres clays
107 (Early Ypresian; 10-15 m thick). The Quaternary silt covers all Meso-Cenozoic formations. In
108 the Deûle valley, the modern alluvial deposits are sand, clay and clayey sand, and locally
109 peat layers and gravel beds. The alluvium is 2 to 5 m thick in the study region. With the
110 "Dièves" as the impermeable base, the upper part of the white Chalk corresponds to the
111 aquifer exploited in the wellfields in the south of Lille Metropolis. Groundwater flows in the
112 Chalk aquifer through a network of faults and open fissures that is well developed at 10-20 m
113 depth, and where the main water inflow occurs (Walaszek et al., 2021). From 1981 to 2010,

114 the average annual rainfall was 742 mm with an effective rainfall of 186 mm (25%), the main
115 recharge area being close to Emmerin.

116 About 30% of the drinking and tap waters for Lille Metropolis is pumped from four main
117 well fields tapping the Chalk aquifer southwest of Lille: Emmerin, Houplin-Ancoisne, Les
118 Ansereuilles and Seclin (Fig. 1). The Emmerin and Houplin-Ancoisne well fields will be
119 referenced hereafter as E-HA, but here we mainly focus on the Les Ansereuilles well field
120 with 26 pumping wells, which is parallel to the Deûle canal. The groundwater, which is
121 unconfined southwest of the Deûle, flows northwest to become confined under the alluvial
122 cover. The A10-A15 well area (Fig. 1) evolves towards local confinement due to the
123 presence of more than 10 m of Tertiary Louvil clays over the Chalk (Cary et al., 2014).

124 The water levels in the study area vary according to pumping and recharge (Fig. 2).
125 The main water direction flows from NE to SW (well A15 to A10). However, there may be,
126 very locally, another flow direction from well A13 towards well A15 as already observed in a
127 hydrodynamic model based on extraction volumes (Bessière et al., 2015) due to high
128 exploitation rates in well A15. The flow in the fractured corridor between A12 and A13 is
129 unknown.



130
 131 *Figure 1: Study site and cross section (RP11) in the well fields of southern Lille. The colour of the*
 132 *pumping wells indicates the maximum concentration of selenium in groundwaters from 2013 to 2017.*
 133 *The piezometric map presents simulated levels with the hydrogeological model.*

134

135 3. Material and methods

136 3.1 Solids analysis

137 Solids were sampled in the Templeuve quarry near the study site and also in a borehole
 138 close to well A13. The samples were ground and dissolved chemically (aqua regia + HF),
 139 and the concentrations were analysed by Inductively Coupled Plasma Mass Spectrometry
 140 (ICP-MS) at BRGM. An extraction sequence with chemicals was used for determining the Se
 141 content in pyrite and the degree of pyritization of Se, based on the work of (Huerta-Diaz and
 142 Morse, 1990): 2.5 g of sediment was placed in contact with a 1M HCl solution to extract the
 143 so-called reactive fraction for 24 hours at room temperature. Though this reactive fraction is

144 generally accepted by the scientific community for divalent metals, it is, however, only
145 indirectly admitted for Se (Peters et al., 1997; Sharma et al., 2014).

146 After centrifugation, the supernatant was recovered for iron and selenium analyses and
147 the solid was again washed with a 10M HF solution at room temperature for 24 hours. This
148 washing step was proposed by Huerta-Diaz and Morse (1990) in order to remove elements
149 that are associated to silicates and alumino-silicates before pyrite extraction. Indeed,
150 concentrated nitric acid used to dissolve pyrite may also result in partial extraction of some
151 elements from silicate phases. It is worth noted that this step is not considered here as a
152 specific extraction and the recovery solution was therefore not analysed. The solid recovered
153 was rinsed with Milli-Q water and finally put in contact with concentrated HNO₃ for 2 hours at
154 room temperature. During this step, the pyrite was solubilized and the selenium extracted. Fe
155 and S were then determined by ICP-AES (Agilent, model 5110 VDV) to quantify the pyrite
156 content and to check that the Fe/S molar ratio was 0.5. Se was determined by ICP-MS
157 (Agilent, model 7900) using a collision-reaction chamber under hydrogen flow and by
158 targeting the ⁷⁸Se isotope. From these extractions, it was possible to calculate the degree of
159 pyritization (DOP, Equation 1) and the degree of trace selenium pyritization (DTSeP,
160 Equation 2) as follows (Huerta-Diaz and Morse, 1990):

161
$$DOP = [Fe]_{pyrite} / ([Fe]_{pyrite} + [Fe]_{HCl}) \text{ (Eq. 1)}$$

162
$$DTSeP = [Se]_{pyrite} / ([Se]_{pyrite} + [Se]_{HCl}) \text{ (Eq. 2)}$$

163

164 **3.2 Water analyses**

165 The initial sampling and analysis work (June 2011 to March 2013) concerned 20 wells as
166 described in Cary et al. (2014). Although a complete chemistry analysis was conducted, only
167 selected data are presented here. Measurements of the physical and chemical parameters
168 (temperature, conductivity, pH, Eh (Pt/Ag AgCl), and dissolved oxygen) were made *in situ*.
169 The groundwater samples were then filtered in the field at 0.45 μm. In the sample sets, the S
170 and Se speciation were determined, with concentrations of total S, S₂O₃, S²⁻, SO₃, total Se,

171 Se(VI) and Se(IV) being measured by HPLC-ICP-MS after separation. Dissolved Fe(II) was
172 analysed in the field by colorimetry. Dosage of total organic carbon (TOC) and dissolved
173 organic carbon (DOC) was carried out on the raw solution after oxidation with sodium
174 persulphate in a hot acid medium. The $\delta^{34}\text{S}$ and $\delta^{18}\text{O}$ of the sulphate were analysed on raw
175 water. The $\delta^{34}\text{S}$ of sulphates was measured from SO_2 obtained from CdS precipitate after
176 SO_4 reduction with addition of cadmium acetate. S and O isotopic compositions were
177 determined on SO_4 using a Delta S mass spectrometer (Thermo Finnigan) with a precision of
178 0.3‰. Isotopic compositions use the usual δ -scale in ‰ according to $\delta_{\text{sample}} (\text{‰}) = (R_{\text{sample}} -$
179 $R_{\text{standard}}/R_{\text{standard}}) * 1000$, where R is the $^{34}\text{S}/^{32}\text{S}$ atom ratio, from V-CDT (Vienna - Canyon
180 Diablo Troilite) isotope ratio standards.

181 The second campaign took place in November 2017, with sampling and water analysis
182 for chemistry, $\delta^{13}\text{C}_{\text{DIC}}$, and gas sampling and analysis. Total DOC was extracted as CO_2 by
183 water sample acidification with H_3PO_4 . The CO_2 extracted under vacuum was purified before
184 analysis by mass spectrometry. Results are given in $\delta^{13}\text{C}_{\text{TDIC}}$ vs. PDB (in ‰). Gases were
185 analysed by the BRGM laboratory using a Trace GC Ultra Thermo Fisher Scientific gas
186 chromatograph (Thermo Scientific, with FID detector). The gases investigated were CO_2 , H_2 ,
187 O_2 , N_2 , H_2S , CH_4 with injection valves of 25 μL and 250 μL . Detection limits were 0.001%
188 (v/v) for CO_2 , O_2 and N_2 , 0.005% (v/v) for H_2 and H_2S , and 0.0002% (v/v) for CH_4 .

189 Finally, available chemical data of the Lille Metropolis were taken from the trimestrial
190 water-quality surveys (2013 to 2017), which only present total Se concentrations.

191 **3.3 Geophysical imaging**

192 Knowledge of the complex organization of geological formations, such as the presence of
193 clays that can induce groundwater confinement and thus the modification of the redox
194 conditions controlling the mobility of selenium, or the fracturing of the chalk that can induce
195 preferential water circulations, is an essential lock. To image the subsurface, we used
196 geophysics, and in particular electrical resistivity tomography. The applied Direct-Current

197 resistivity method, imaging the resistivity distribution in the subsurface, is widely used for
198 hydrogeological purposes (Revil et al., 2012) and references therein).

199 A 2-D resistivity profile (RP) was measured in August 2019 about 200 m to the northwest
200 of the Ansereuilles well field, from well A10 to well A15 (RP11, Fig. 1). For data acquisition, a
201 multi-electrode Syscal Pro Switch system (IRIS Instruments) was connected to 96 stainless
202 electrodes 5 m apart. Both dipole-dipole and reciprocal Wenner-Schlumberger arrays were
203 considered; the former for its good resolution of surface levels and lateral resistivity
204 variations, the latter for its sensitivity to vertical resistivity variations that clearly identify
205 horizontal geological levels (Loke, 2015). After data filtering ($V_{\min} \geq 0.1$ mV, $I_{\min} \geq 20$ mA, Q
206 $\leq 5\%$), the electrode topography was incorporated. The Chalk roof and Dièves roof interfaces
207 from the 3-D geological model of the study area (Picot and Bourgine, 2010) were also
208 included to improve the results. Then, a robust-type inversion with RES2DINV software (ver.
209 4.10) was run (Loke, 2020). The RMS error of the resulting resistivity section was 5.8% after
210 five iterations. Interpretation of the 2-D resistivity model was supported by the drilling logs of
211 wells A10 to A15 (BSS, BRGM) and the geological map (Desoignies and Sangnier, 1968).

212 **4. Results**

213 **4.1 Geological setting**

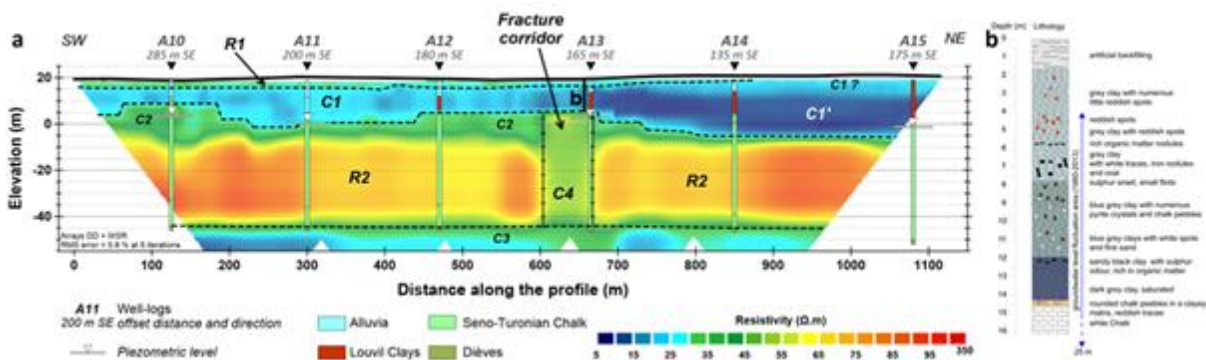
214 For the Quaternary formations, the surface R1 layer (1 to 5 m thick) is moderately resistive at
215 30-35 Ωm (Fig. 2). Mostly consisting of Quaternary silt (Desoignies and Sangnier, 1968),
216 resistivity values in R1 near the Deûle River (300-350 m) suggest a rather sandy facies.

217 The underlying conductive C1 horizon has a resistivity below 20-25 Ωm and mostly
218 consists of Quaternary alluvium. It is on average 10 m thick (Desoignies and Sangnier,
219 1968), but locally varies from 5 to 15 m, according to undulations in the roof of the
220 underlying horizon. Quaternary alluvium mainly is found in the southwest part of the RP11
221 profile; it is exposed to the northeast and its thickness is difficult to evaluate. Here, C1 lies on
222 the highly conductive C1' horizon with an average resistivity below 5 Ωm . According to the

223 numerous drill logs available along the profile, C1' corresponds to the Louvil Clay (Thanetian,
 224 Eocene).

225 For the Senonian-Turonian Chalk and the Dièves, the C2 layer is moderately
 226 resistive, between 25 and 50 Ωm (Fig. 2). Below, the R2 unit shows resistivity values over
 227 50-60 Ωm . From a lithological viewpoint, both C2 and R2 units correspond to the Senonian-
 228 Turonian Chalk. Although the roof of the C2 layer is very irregular along the profile, we
 229 observed a progressive deepening from SW to NE whose maximum amplitude is about
 230 15 m. Within the R2 resistive unit, we noted a 60-m-wide area where the resistivity slightly
 231 decreases ($\sim 30 \Omega\text{m}$, C2') close to well A13 (abscissae 600 to 660 m on Fig. 2). Finally, the
 232 C3 conductive horizon has a resistivity of less than 25 Ωm , being the electrical substratum of
 233 the resistivity section. Analysis of the drill logs indicates that this layer corresponds to Lower
 234 Turonian (Dièves) marl.

235



236

237 *Figure 2: a) 2-D resistivity inversion model along the RP11 profile in Les Anseveilles well field*
 238 *measured in August 2019, and static water levels measured on 31/08/2019 (see Fig. 1 for the location*
 239 *of the RP profile) ; b) Description of the lithology from a drill log near well A13*

240

241 4.2 Selenium in the geological formations

242 The Chalk formation of the Templeuve quarry had Se contents below the quantification limit
 243 ($QL=1 \text{ mg kg}^{-1}$) whereas the Tertiary and Quaternary formations contained relatively high Se
 244 concentrations (Table 1). The highest Se values, 3.57 and 4.87 mg kg^{-1} , were measured in
 245 the upper part of the Thanetian Ostricourt Sand and in the Ypresian Orchies Clay,

246 respectively. Quaternary silt had rather high Se contents (4.1 mg kg^{-1}). Total organic carbon
247 content was 0.27% in Quaternary silt and 0.5% in the Ypresian clay. X-ray diffraction (XRD)
248 patterns of the Chalk show over 99% calcite, traces of quartz ($\sim 1\%$) and, in the reddish parts
249 of the Chalk, traces of siderite and possibly hematite. Ypresian clay and the top of the
250 Thanetian sand show XRD patterns indicating a large presence of quartz and illite, together
251 with pyrite.

252 More locally, the samples at 11.8, 13.3 and 14.2 m depth of the borehole at well A13
253 (Table 1) contain an assemblage of zeolite (7-19%), smectite (69-84%) and opal-CT already
254 described in the British Thanetian (Huggett and Knox, 2006) that may be a typical
255 assemblage of this age, confirming the hypothesis that the clay overlying Chalk in Les
256 Ansereuilles is Thanetian Louvil Clay ((Cary et al., 2014) . The other minerals in the $<2 \mu\text{m}$
257 fraction below 11.8 m, are illite (8-11%), chlorite (1-2%) and quartz. The samples contained
258 up to 4.6 mg kg^{-1} Se at the bottom of the profile, above the Chalk at 13 m depth (Table 1).
259 High Se levels (4.8 mg kg^{-1}) were also found in the banks around well A13, consisting of ash
260 waste from the old thermal plant. At 8.5 m depth, solids are enriched in Fe (7.5%), Se
261 (3.9 mg kg^{-1}) and organic matter (0.54%).

262 Pyrite grains, up to 5 mm large, were found between 7 and 14 m depth in well A13.
263 Both fine-grained and coarser sediments at this depth range contain up to 0.85 wt% pyrite
264 according to the semi-quantitative XRD patterns. The largest pyrite grains were sampled
265 manually at 7, 8.5 and 8.8 m depth; after washing the grains with acid solutions (see
266 previous section), the selenium concentration was estimated for nine replicates of different
267 pyrite-grain samples. We found a Se concentration of 1.2 mg kg^{-1} with an RSD of 22%. In
268 raw sediment, several chemical extractions were needed for understanding the Se
269 distribution, especially as related to pyritic compounds (Table 1, Fig. 2). Se concentrations in
270 pyrite are generally below 0.01%, except in the A13 sample at 5.5 m depth where the
271 maximum content is observed (1.1%). Overall, these concentrations are higher than the
272 values measured in well-crystallized pyrite grains. Table 1 shows that a significant fraction of
273 total Se is included in pyrite with values between 6 and 29% (see Fig. 2 of SI). The DTSeP is

274 still higher (35-74%), meaning that the “mobile Se” (defined by the fraction extracted with a
275 1 M HCl solution) is well trapped in the pyrite fraction (see Fig. 2 of SI).

276 *Table 1: Chemical composition (bulk) and mineralogy (bulk and <2 μm fraction)*
277 *of the regional and local geological formations (sampled at the vicinity of well A13).*
278

279 **4.3 Spatial and temporal variability of groundwater chemistry**

280 The results are presented in Table 2 and on Figs 3 and 4, the sampling points being
281 shown on Fig. 1. Groundwater displayed pH varying from 6.8 (well A4) to 7.3 (well A24). The
282 redox potential varied from 177 mV (well A26) to 460 mV (well E5, Emmerin). The physical
283 and chemical parameters of the groundwater showed a significant spatial variability. The E-
284 HA groundwater had low SO_4^{2-} and high NO_3^- concentrations, but the groundwater of the
285 confined end-member (wells A25 to A28) stood out in having high Cl and SO_4^{2-}
286 concentrations. Comparatively, the groundwater in wells A12 and A13 had high SO_4^{2-} and low
287 NO_3^- concentrations. For each point, time variations are represented by the range of values
288 in Figs 3 and 4; they are best expressed for Se values in the wells of the redox sequence,
289 where Se contents can double during a year.

290 For S speciation, S^{2-} and $\text{S}_2\text{O}_3^{2-}$ were measured <QL, whereas low amounts of SO_3^{2-}
291 were found in most groundwater samples (not shown in Table 2). For Se speciation, all
292 groundwater samples had Se(VI) concentrations at levels over the QL. Only the groundwater
293 in wells A12 and A13 had low amounts of Se(IV) ($0.27\text{-}1.39 \mu\text{g L}^{-1}$), Se(VI) being the major
294 aqueous phase. Table 3 shows dissolved gas values in 7 wells of the redox sequence and
295 three wells of the catchment. Methane is present in increasing concentrations from wells A12
296 to A15, but absent elsewhere. Well A13 contains clear peaks of CO_2 and O_2 , but less N_2 than
297 in the other wells.

298 *Table 2: Physical and chemical composition of groundwater samples from 2011 to 2019. DO is*
299 *dissolved oxygen. TOC is for Total Organic Carbon. The precision is $\pm 0.3\%$ on $\delta^{18}\text{O}_{\text{SO}_4}$ and $\delta^{34}\text{S}_{\text{SO}_4}$*
300 *and $0.1 \mu\text{g L}^{-1}$ on Se(VI) and Se(IV).*

301

302

Table 3: Gas concentrations in groundwater sampled in November 2017.

303

304 **4.4 The $\delta^{34}\text{S}$ and $\delta^{18}\text{O}$ isotopic composition of groundwater**

305 The Emmerin groundwaters have positive isotopic compositions for $\delta^{34}\text{S}$ and $\delta^{18}\text{O}$ of
306 sulphate, whereas all other groundwaters show negative $\delta^{34}\text{S}$ (Table 2). Houplin-Ancoisne
307 groundwaters show a high variability of $\delta^{34}\text{S}$ (-30 to -5‰ including error bars) and $\delta^{18}\text{O}$ (0 to
308 6‰) during the whole monitoring year, similar to those observed in the Les Ansereuilles well
309 field that shows $\delta^{34}\text{S}$ varying from -27.4‰ (A12) to -5.7‰ (A23). Monthly monitoring of well
310 A13 showed a stable $\delta^{34}\text{S}$ ($\delta^{34}\text{S}$ close to -20‰) and $\delta^{18}\text{O}$ variations (around 6‰). A decrease
311 of $\delta^{18}\text{O}$ values occurred in groundwater from February to May, followed by an increase until
312 next winter with the highest $\delta^{18}\text{O}$ in February-March, back to the initial values.

313 **5. Discussion**

314 **5.1 Geophysics and hydrogeology**

315 The geophysical results highlight two essential elements from a hydrogeological point of
316 view. First, they confirm the presence of Louvil Clays (C1') and define their geometry (Fig 2).
317 To the southwest, these clays are lenticular within recent alluvial deposits (C1) and evolve
318 into a continuous level to the northeast, thanks to a deepening of the underlying horizon. The
319 transition between Quaternary alluvium and Louvil Clays is progressive, and we cannot
320 define a precise limit between those two units. This thickening of the Louvil Clays leads to a
321 progressive confinement of the Chalk aquifer from southwest to northeast.

322 Beyond the 600 m abscissa, the Louvil Clays are 7 to 15 m thick according to the well
323 logs (A13, A14 and A15, Fig. 2), but the thickness of the corresponding C1' electrical horizon
324 varies from 10 m (A13) to about 20 m (A14, A15). The upper conductive part of the Chalk
325 (C2) corresponds to its weathering-related fractured and productive part (Portal et al.,
326 submitted). Starting at well A13, we suggest that the very low resistivities in the upper part of
327 the Chalk are due to the presence of Louvil clay that may have infiltrated the underlying
328 Chalk and settled along the walls of the macro- and microporosity. This clay coating could

329 explain the low resistivities observed for weathered Chalk in this area. It also has strong
330 hydrogeological consequences, as it contributes to increasing water-residence time and thus
331 enhances water-rock interactions.

332 Secondly, geophysics show a local resistivity decrease (C2') into the resistive Chalk
333 (R2, Fig. 2). We interpret this 60-m-wide area as a large fracture corridor. Such structures
334 are well known in basement contexts (Acworth, 1987) and their more conductive signature,
335 compared to that of fresh basement rock, had already been observed (Belle et al., 2019;
336 Comte et al., 2012; Descloitres et al., 2008). To our knowledge, few other geophysical
337 studies have focused on the Chalk aquifer, probably because it is an easily exploitable water
338 resource. However, recent work on the hydrogeological setting of the Chalk aquifer in
339 Normandy (France) has highlighted similar multi-decamic zones of resistivity decrease
340 within the resistive Chalk, related to regional or local faults (Meire et al., 2019; Portal et al.,
341 2020). The geophysical anomaly identified close to well A13 may result from alteration due to
342 the presence of faults. It probably extends on either side of the RP11 profile, following a
343 N110-N130 orientation inherited from the regional trend of Carboniferous basement tectonic
344 structures, thus constituting a preferential groundwater circulation pathway that may favour
345 the mixing of groundwaters of different origins under the impulse of pumping.

346 **5.2 Se contents in rock**

347 The geological units of the northern region show heterogeneous Se contents, comparable to
348 those of the formations of the whole Paris Basin (Table 1). Whereas Ypresian clay commonly
349 has the highest Se concentrations of Paris Basin sediments (695 mg kg⁻¹ in Lower Ypresian
350 lignitic Black Sands, 11.8 mg kg⁻¹ in Lower Ypresian Clay (Gourcy et al., 2011), the Se
351 contents of the Tertiary and Quaternary formations in the Lille region are much lower (4.6-4.9
352 mg kg⁻¹). Moreover, the highest Se values of the study area are found in basal Thanetian
353 Louvil Clays overlying the Chalk (4-4.6 mg kg⁻¹). The Se content of Quaternary silt in the Lille
354 region is clearly higher than that observed in agricultural soil developed on Quaternary
355 deposits in Belgium, ranging from 0.1 to 0.7 mg kg⁻¹ (De Temmerman et al., 2014). Overall,

356 the soils of northern France and Belgium are known to be Se-depleted, the Se being
357 supplied by Se-rich mineral fertilizers, containing up to 200 mg kg⁻¹ Se, as well as animal
358 manure (ADEME, 2007) to ensure correct Se contents in wheat.

359 The “primary” presence of Se is indeed linked to Quaternary deposits when present
360 (e.g., aerial loess vs. erosion of Tertiary Se-enriched sediments), and local ‘hot spots’ of Se-
361 enriched soil reaching 1 mg kg⁻¹ are known in the north-eastern part of the Paris Basin
362 including the Lille region (Baize et al., 2010). Generally speaking, the Se content of bedrock
363 and soil in the Lille region is comparable to that of other Se-rich geological regions in the
364 world and can present Se values over 1 mg kg⁻¹, which is considered as the toxic level
365 (Bailey, 2016). The processes leading to high Se concentrations in groundwater thus remain
366 to be understood.

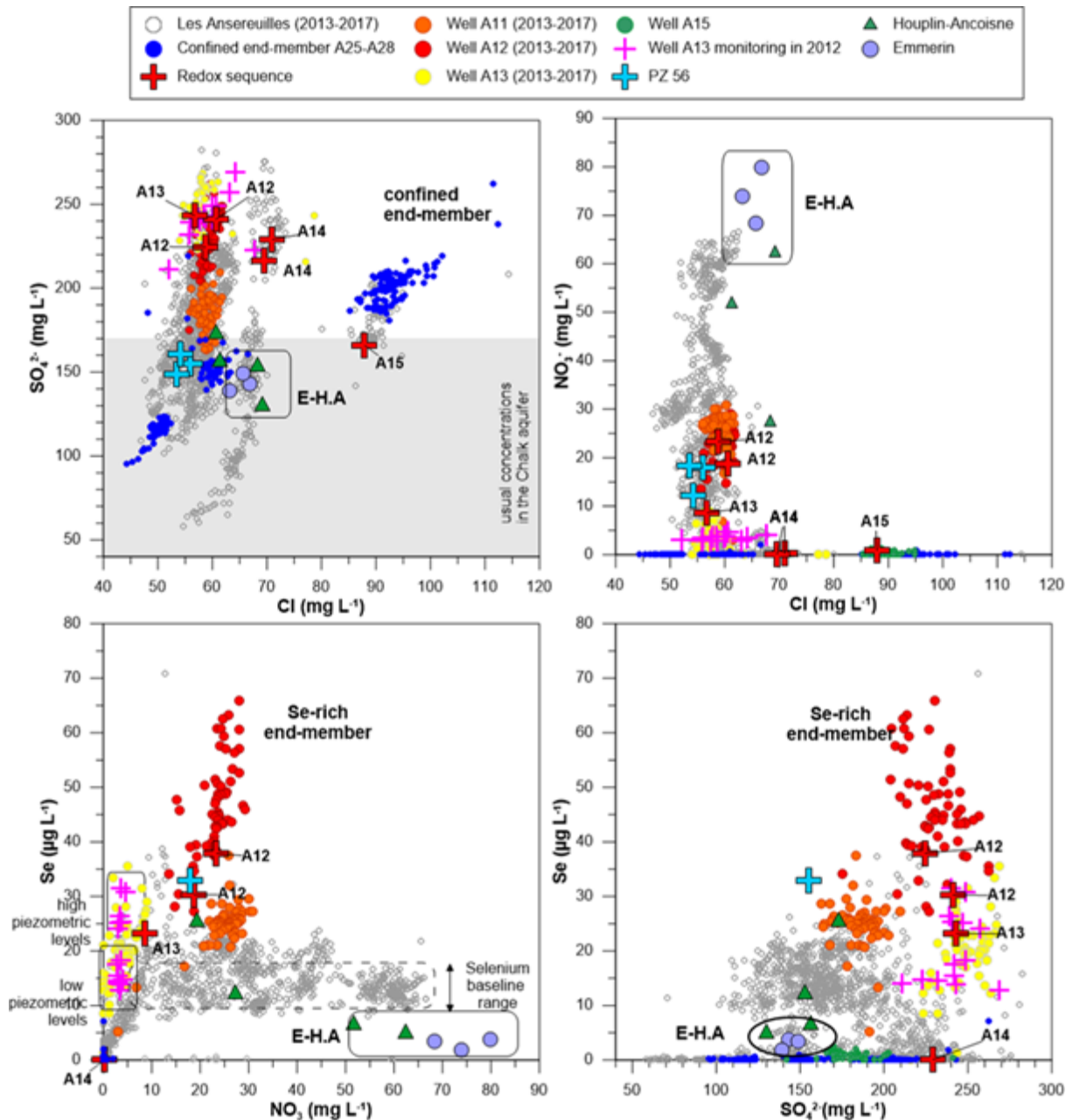
367 **5.3 The local Chalk groundwater chemistry**

368 The chemical facies of the groundwater samples are bicarbonate-calcium type (Ca-Mg-
369 HCO₃, see Piper diagram in Fig. 1 in Supporting Information) and evolve between two facies
370 (Fig 3): (1) the upstream oxic E-HA groundwater type where dissolved O₂ varies from 4.8 to
371 8.9 mg L⁻¹, with high NO₃ and low sulphate concentrations; and (2) the confined type with
372 semi-oxic groundwater of well A26 under continuous Tertiary cover, with a very low O₂
373 content (0.3 mg L⁻¹), a nitrate content <QL and high sulphate concentrations indicating
374 denitrification and a long residence time with long water-rock interaction (Cary et al., 2014).
375 The pH range is similar to that in other parts of the unconfined Chalk aquifer in France and
376 England (Edmunds et al., 1987; Négrel and Petelet-Giraud, 2005).

377 HCO₃ contents vary between 256 and 506 mg L⁻¹, the lowest values occurring in the
378 Emmerin well field and the highest in well A13 (Table 2). These values are above the usual
379 ones in the English Chalk aquifer (Edmunds et al., 2003), in the Somme region (Négrel and
380 Petelet-Giraud, 2005), or in the south of the Paris Basin (Brenot et al., 2008). Similarly,
381 sulphate concentrations in the study site are all above the ones measured in the Chalk
382 aquifer in the Somme (Négrel and Petelet-Giraud, 2005; Fig. 3). The sulphate content in

383 wells A12 and A13 is higher than the threshold value in English Chalk (Edmunds et al.,
384 2003).

385 Compared to the general trend in the Chalk aquifer in France and the UK, the higher
386 mineralization in the Lille region probably originates from exchange with the underlying
387 Carboniferous aquifer and/or the overlying Tertiary sediments. Here, at around 100 m depth
388 below the Chalk in the studied well fields, the Carboniferous contains Viséan evaporites and
389 its groundwater is highly mineralized (Bernard et al., 1981). Upwelling of mineralized fluids
390 may occur through deep-seated faults in the basement and Chalk, particularly near the study
391 site, but this hypothesis has not yet been proven. However, the role of Tertiary sands and
392 clays as sources of mineralization of the Chalk aquifer (Bernard, 1979) is coherent with the
393 high K ($>15 \text{ mg L}^{-1}$) and SO_4 ($> 100 \text{ mg L}^{-1}$) values observed in wells tapping the confined
394 Chalk (wells A25 to A28, Fig. 3 and Table 2). Interestingly, in spite of the reductive conditions
395 in this confined part of the aquifer and sufficient available organic carbon (1.35 mg L^{-1}), SO_4^{2-}
396 remains present in groundwater.



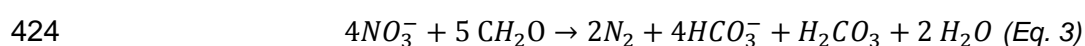
397
 398 *Figure 3: Binary diagrams showing element concentrations in the groundwater of the Chalk aquifer at*
 399 *the study site. All circles are from the quality monitoring of the EML from 2013 to 2017; all other points*
 400 *were acquired in 2011- 2013 and 2017-2019.*

401

402 **5.4 Geochemical processes of the redox sequence**

403 The continuum of wells A16-A11-A12-A13-A14-A15 along the Deûle channel constitutes a
 404 remarkable redox sequence (Fig. 4) over a very short distance (1600 m). Plotting data
 405 chronicles from Lille Metropolis for 2013-2017 and recent monitoring studies, shows that the
 406 range of concentrations of each parameter is large as it varies with time under the

407 constraints of natural recharge and pumping. The general transition from oxic to anoxic
 408 conditions, driven by clay overlying the Chalk, is rapid but progressive, and the increase in
 409 reductive conditions strictly respects the sequence of microbially mediated oxidation-
 410 reduction reactions. Thus increase represents the thermodynamic order of the reactions
 411 $O^0/O^{-II} > N^V/N^0 > Se^{VI}/Se^{IV} > Mn^{IV}/Mn^{II} > Fe^{III}/Fe^{II} > S^{VI}/S^{IV}$ (Stumm and Morgan, 1996), as
 412 already described from England (Edmunds et al., 1987). The measured O_2 -content range is
 413 typically included in the respiration threshold (0.03 - 2.0 mg L^{-1}), indicating a transition state
 414 between the oxidation of organic matter by oxygen and by nitrate (Ashok and Subrata, 2015).
 415 Confined conditions cause very low O_2 content (0.26 to 0.50 mg L^{-1} , Fig. 4) and nitrate tends
 416 to be reduced (from 25 - 30 mg L^{-1} in A16 to $<QL$ in A14 and A15) with the production of NH_4
 417 (mean of 0.55 mg L^{-1} in well A14) and traces of NO_2^- (Fig. 4). Reduction of nitrate can be
 418 associated with oxidation of organic matter, but also with oxidation of reduced minerals
 419 (Parmentier et al., 2014), as pyrite was identified in Thanetian clay. Organic carbon is
 420 present in the clayey sediment (0.35 – 1.80% dw) overlying the Chalk, and also occurs in
 421 aqueous phase in well A13 (1.5 to 3.2 mg L^{-1}). Assuming that this organic matter is
 422 bioavailable for bacterial metabolism, its oxidation produces inorganic carbon according to
 423 the reaction given in Equation 3:

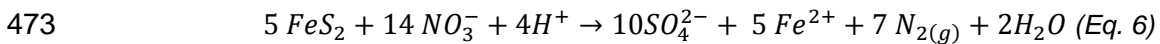
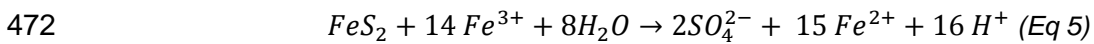
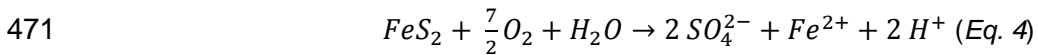


425 The organic matter was modelled as CH_2O , although natural organic matter can exhibit
 426 different formulae; the resulting production of protons should be different. The production of
 427 N_2 is proven with high values in wells A12 and A13 (1.3 and 1.4 mmol L^{-1} , respectively, Table
 428 3), which are higher than those of E-HA, except for well H11. A denitrification process as in
 429 Equation 3 typically goes through a temporary production stage of NO_2^- and leading to the
 430 final production of NH_4^+ , both of which have been identified in groundwater samples.
 431 Oxidation of organic matter acidifies the system, but no notable acidification was found in
 432 well A13, where the pH range is 6.8 - 7.3 , or in the other studied wells (Table 2). The pH is
 433 probably buffered by calcite dissolution from Chalk, which explains the high Ca contents of

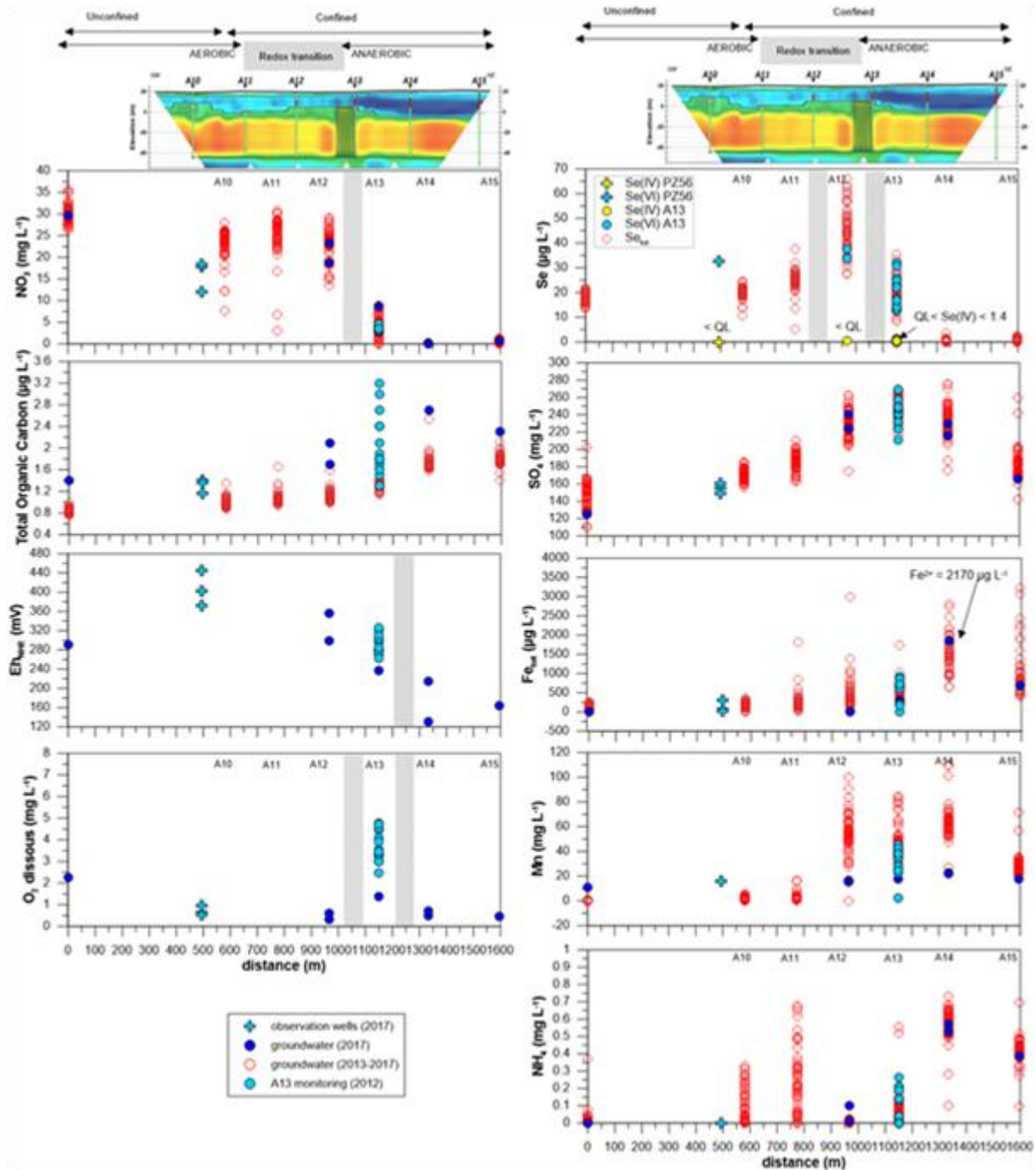
434 wells A12, A13, A14 and A15 compared to the other Les Ansereuilles wells (Cary et al.,
435 2014; Table 2). The production of HCO_3^- according to Equation 2 can contribute to the
436 relatively high content observed in the studied groundwater. Better to assess the HCO_3^-
437 origin, the $\delta^{13}\text{C}$ of dissolved inorganic carbon was measured on some samples, ranging from
438 -14.20‰ to -11.6‰ with a pH ranging from 6.73 to 7.1. These values are typical of the Chalk
439 aquifer in unconfined or semi-confined conditions, and are interpreted as resulting from
440 dissolution of the carbonate matrix (Kloppmann et al., 1998). The concentrations of dissolved
441 manganese increase in groundwater along the transect A16 to A15, with a maximum in well
442 A12. Dissolved iron concentrations follow the same trend with a general increase reaching
443 the highest values in well A14. Mn- and Fe-oxihydroxides reduction is most probably the
444 main process here. The presence of dissolved methane in wells A12-A13-A15 (Table 3)
445 confirms that organic matter is probably first biologically or chemically degraded in CO_2 , and
446 then reduced by CH_4 , although the measured redox potential does not represent a CH_4/CO_2
447 couple or a very reductive system.

448 The continuum of wells shows high SO_4^{2-} values associated with high Se values and
449 low NO_3^- values (Fig. 3). However, such high Se concentrations are not coherent with the
450 local reductive conditions, so we suspect another process than reduction to be active here as
451 well. An oxidation reaction may be the main process here; a very interesting element of this
452 redox sequence is that an oxidative flow crosses a progressively settled anoxic state. Indeed,
453 the monthly monitoring of well A13 showed dissolved O_2 content varying with time from 2.5 to
454 4.8 mg L^{-1} , these values being higher than those in wells A12 or A14 (Table 3; Fig. 4). We
455 can thus assume that dissolved O_2 is probably introduced in the system by water flowing
456 through the fractured corridor near A13 (Fig. 2). The introduction of dissolved O_2
457 superimposes a secondary “oxidation sequence” on the predominant reduction reactions.
458 Such oxidation reactions laterally are effective over short distances, governed by flow
459 direction and groundwater mixing, and by the reaction rates, as illustrated by the low
460 dissolved O_2 content in wells A12 and A14 (Table 2; Fig. 4). The slight decrease of dissolved

461 iron in well A13, mainly as Fe(II), can be linked to the presence of dissolved oxygen causing
 462 Fe(III)-oxide precipitation (Fig. 4), even if chemical Fe(II) oxidation can also occur under
 463 anaerobic conditions in the presence of Mn(IV), NO_3^- , and NO_2^- (Kappler and Straub, 2005).
 464 Illustrated by the slight decrease in dissolved Fe- and Mn concentrations, the best
 465 expression of oxidation are the high values of SO_4^{2-} and Se concentrations, mainly as Se(VI),
 466 in well A12 (Fig. 4). The presence of a certain amount of dissolved O_2 in A13 makes pyrite
 467 oxidation possible (Eq. 4), present in reducing environments and commonly identified in
 468 Chalk porosity (Edmunds et al., 1987). It also leads to the presence of Fe^{2+} (Eqs 4 and 5)
 469 further oxidized into Fe(III), and NO_3^- reduction (Eq. 6) resulting in the high SO_4^{2-}
 470 concentrations of wells A13 and A12, and in denitrification (Zhang et al., 2012).



474 SO_3^{2-} , a product of pyrite oxidation found in well A14 at low levels, is not stable and
 475 rapidly oxidizes to sulphate in the presence of oxygen or any other oxidizing agent. Acidity
 476 produced in Eq. 4 and 5 would be buffered by calcite dissolution.



477
 478 *Figure 4: Redox sequence in the Les Anseveilles field well presenting the geophysical profile and the*
 479 *chemical composition of groundwater in each well. Distance is calculated relative to well A10.*
 480 *PZ56 is not in the continuum, but slightly southeast under the same geological conditions.*
 481

482 It is worth noting that the processes within the water-level fluctuation zone are dynamic
 483 and that the redox front position varies with time, laterally but also vertically, in the water-
 484 level fluctuation zone. The oxidation processes linked to mixing with oxic waters are
 485 distributed laterally around well A13 according to the main flow driven by pumping. Towards

486 well A15 under complete reduced conditions, O_2 and NO_3^- will be rapidly reduced, whereas
487 towards A12, which is not denitrified, the mixing slows down the creation of reductive
488 conditions. This example provides an interesting illustration of the complex “permanent”
489 transient states of groundwater.

490 **5.5 Constraints related to the isotopic composition of sulphate molecules** 491 **in groundwater**

492 In the Chalk aquifer near Lille, several potential sources of dissolved sulphates can be
493 identified. The $\delta^{34}S_{SO_4}$ in E-HA well fields (+0.4 to +1.6‰) most likely originates from
494 atmospheric deposition and fertilizers (-6 to +21‰), (Vitòria et al., 2008) (Table 2). For the
495 other groundwater samples, a large variability of negative $\delta^{34}S$ values is noticed between
496 wells (Figs. 6 and 7), matching the general composition of pyrite (Thode, 1991), of local
497 pyrite and local solid Chalk (respectively $\delta^{34}S_{SO_4}$ of -20‰, and -10 to 15‰; Simon, 1986)).

498 The first hypothesis lies in a mixing between the E-HA pole and the T-Q end-member
499 as defined in Cary et al. (2014), with $\delta^{34}S$ of Louvil Clays: -37 to -40‰ (Bernard et al., 1981).
500 The negative values of sedimentary sulphides in the T-Q end-member are coherent with their
501 marine origin. In the redox sequence (Fig. 5) where only Louvil clay is present, the mixing
502 line correctly fits values of wells A15, A26 and E-HA, but it does not explain all the points. A
503 SO_4^{2-} excess is found in well A14, and a deficit for PZ56 and A12. The annual variability of
504 $\delta^{34}S$ in well A13 is not completely explained; some points belong to the general area of
505 sulphates deriving from pyrite dissolution, and other points correspond to the sulphate
506 reduction line (Figs 6a and b). As pumping induces groundwater mixing, the decreasing and
507 variable rates of oxidized water reaching wells A12, A13 and A14 through the fractures of the
508 corridor should constrain the processes controlling $\delta^{34}S_{SO_4}$ and SO_4 concentrations.

509 The second hypothesis then must consider fractionation processes. All the wells of the
510 redox sequence are well explained by the reduction line (slope -2, Figs 6a and b). The
511 observed increase in $\delta^{34}S_{SO_4}$ (+16.8‰) and $\delta^{18}O$ (+ 4.5‰) from wells A12 to A15 is
512 interpreted as resulting from kinetic S-isotope fractionation enhanced by bacterial sulphate

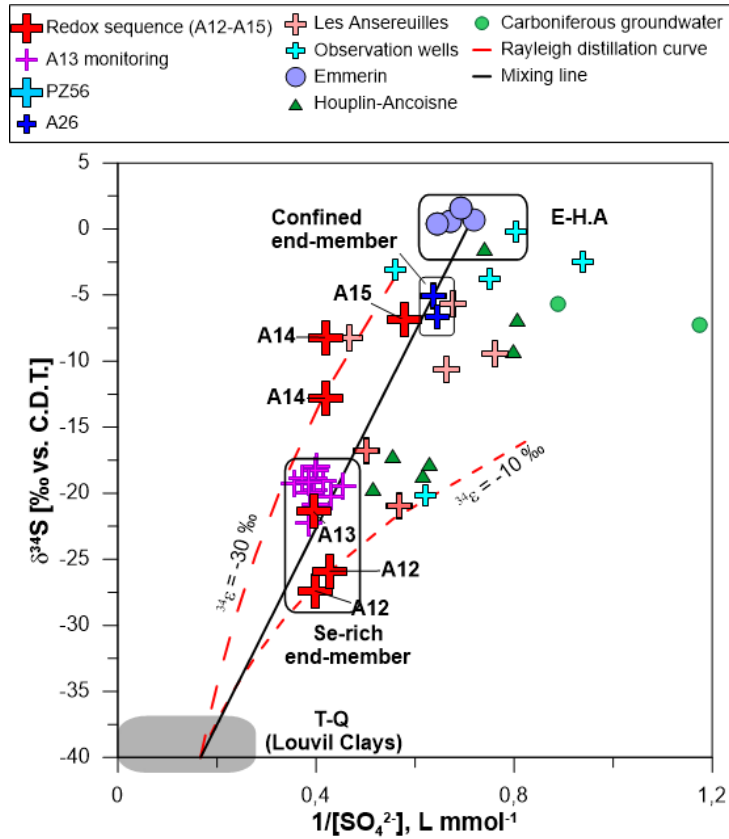
513 reduction, causing a preferential enrichment in ^{34}S and ^{18}O in the residual SO_4^{2-} . The
514 Rayleigh equation (Mariotti et al., 1988) can be used to describe isotope fractionation :

515
$$\delta_r = \delta_0 + \varepsilon \ln \frac{C}{C_0} \text{ (Eq. 7)}$$

516 where δ_r and δ_0 are residual and initial sulphate reservoirs, ε is the isotopic enrichment factor
517 and C/C_0 is the remaining sulphate fraction. The Rayleigh equation was calculated for ε -
518 30‰ and -10‰ with the T-Q end-member as the initial source. This range of ε may represent
519 a natural variability of conditions, with various rates of fractioning due to evolving redox
520 conditions and processes (Detmers et al., 2001). All points are correctly explained by the
521 range included in the two curves modelling bacterial sulphate reduction. The enrichment
522 factor of -10‰ explains the composition of PZ56 and well A12, whereas that of -30‰ better
523 corresponds to the other wells of the sequence. This difference may be due to the fact that
524 PZ56 and well A12 are not pumped, contrary to the other wells. It is possible that alternating
525 oxidation-reduction cycles caused by pumping enhance the reduction process beyond
526 normal denitrification and Fe-oxide dissolution. We expect that this effect is less visible in the
527 non-exploited wells.

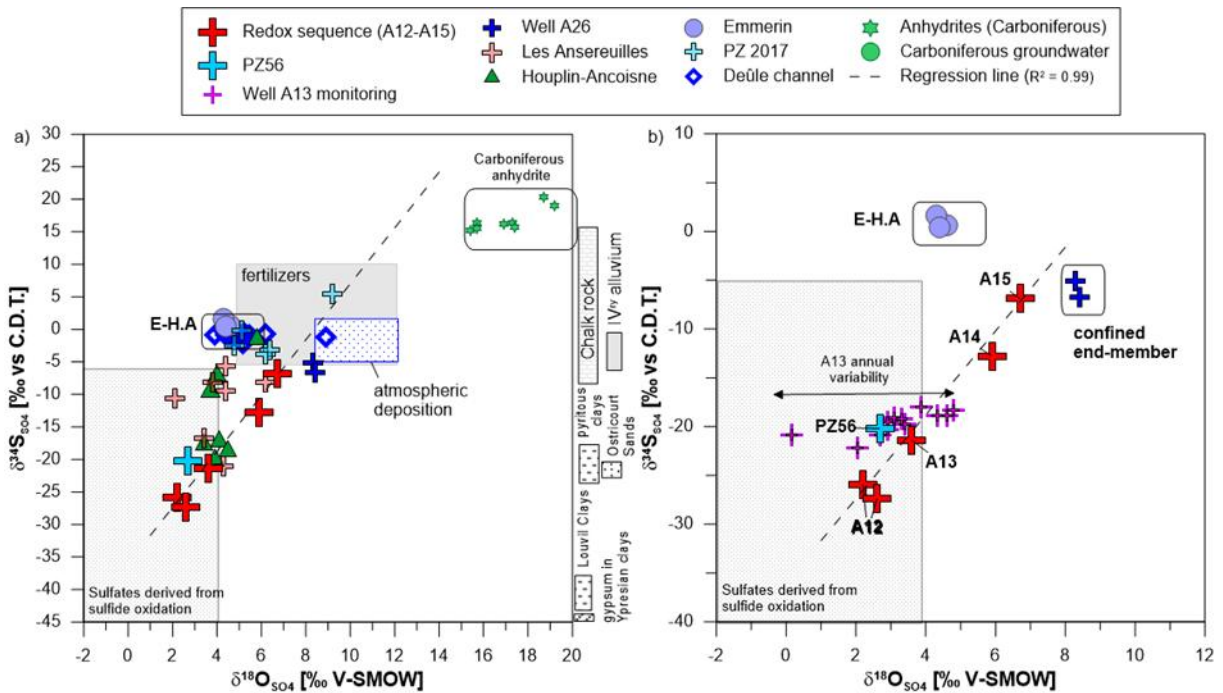
528 However, SO_4^{2-} concentrations in wells A12-A13-A14 are expected to decrease with
529 increasing reducing conditions, as is the case for A15, but they do not vary significantly (Fig
530 5). This means that, although SO_4^{2-} is reduced by microorganisms, this may be compensated
531 by an increase in the contribution of pyrite oxidation in wells A12 and A13. The low variability
532 of the $\delta^{34}\text{S}_{\text{SO}_4}$ of sulphates is observed in wells A13 (n=13) and A12 (n=2) data, because
533 sulphur isotopes essentially undergo no fractionation during pyrite oxidation to sulphate (Van
534 Stempvoort et al., 1994).

535



536
537
538
539

Figure 5: Variations of $\delta^{34}\text{S}$ (normalized to Vienna Canyon Diablo Troilite) of sulphate molecules in groundwaters versus $1/\text{SO}_4^{2-}$ from the well fields of southern Lille. Data from Carboniferous groundwater are from Gourcy et al. (2013). The error bar is within the point.



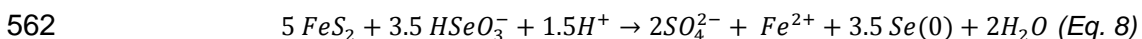
540
541
542
543

Figure 6: a) $\delta^{34}\text{S}_{\text{SO}_4}$ vs $\delta^{18}\text{O}_{\text{SO}_4}$ in groundwater from the well fields (2011-2017) and monitoring data of well A13; b) Zoom on the redox sequence area. Bibliographic data are from (Bernard, 1979; Gourcy et al., 2013; Simon, 1986). The error bar is within the point.

544 **5.6 Processes driving selenium speciation and mobility**

545 In the redox sequence of Les Ansereuilles, the general scheme of Se concentrations in
546 groundwater shows Se values around 20 µg L⁻¹ under oxic conditions that evolve to very low
547 values under progressively reducing conditions (MEL data of Fig. 4; Table 2). As expected,
548 Se(VI) is the main inorganic Se form in these groundwaters, except for wells A12 and A13
549 where low Se(IV) concentration values were detected (Fig. 4 and Table 2). This is coherent,
550 as reducing conditions promote the reduction of Se(VI) and Se(IV) ions to insoluble
551 elemental Se(0). In spite of this general scheme, a large increase in Se concentrations in
552 well A12 and, to a lesser extent, in A11 and A13, was noted (Figs. 3 and 4).

553 As already mentioned for the sulphur cycle, the mixing with oxidized water flowing from
554 the fracture corridor probably superimposes oxidation of reduced Se species, pyrite playing a
555 major role in controlling Se mobility and speciation. As part of the general redox sequence,
556 the creation of reducing conditions imposes simultaneous reduction of NO₃, Se(VI) and SO₄²⁻
557 that significantly removes Se from water (Nkansah-Boadu, 2019; Oremland et al., 1999; Tan
558 et al., 2018). Precipitation of pyrite induces reduction of soluble Se(IV) and Se(VI) (Mitchell et
559 al., 2013), and Se adsorption or incorporation in the crystal lattice (Diehl et al., 2012; Naveau
560 et al., 2007). The reduction of aqueous Se(IV) by pyrite is dominated by the following
561 reaction in Equation 8 (Kang et al., 2011):



563 In addition, Se(-II) can be immobilized on the surface of pyrite as a result of a reduction
564 reaction, leading to the formation of Se(0) (Liu et al., 2008). Se(0) can also be transformed to
565 FeSe₂ (ferroselite) with the depletion of Se(IV) (Kang et al., 2016). Not detected in the Louvil
566 Clays, perhaps because of its presence in very small amounts, FeSe₂ that precipitates under
567 reducing conditions in anoxic environments (Ryser et al., 2005), may be present in the
568 water-level fluctuation area in the Chalk. Under the local oxidizing conditions induced by
569 groundwater mixing and in view of the values in the nearby Houplin-Ancoisne well field (Fig
570 3), we can assume that the oxidizing groundwater may contribute a certain amount of Se

571 (probably around $10 \mu\text{g L}^{-1}$) and nitrate ($60\text{-}70 \text{ mg L}^{-1}$) from the local geochemical
572 background. Furthermore, organic matter can be degraded by aerobic heterotrophic bacteria,
573 releasing Se that was complexed with insoluble organic molecules, as illustrated by the
574 presence of organic carbon (DOC 1.7 to 2.9 mg L^{-1}) in groundwater of well A13. Se(IV)
575 adsorption with Fe-Mn-oxide precipitation potentially is another major process (Xu et al.,
576 2020).

577 The highest Se values are found with low amounts of dissolved O_2 ($0.5\text{-}4 \text{ mg L}^{-1}$) and
578 nitrate ($15\text{-}30 \text{ mg L}^{-1}$), but high SO_4^{2-} values ($>170 \text{ mg L}^{-1}$; Fig. 3). This range of values
579 reflects the nitrate reduction area, which is accompanied by oxidation of Se-bearing pyrite
580 and of Se reduced phases produced by microorganisms during an earlier anoxic phase.
581 Indeed, Se included in sulphides—pyrite, marcasite or mackinawite—can be released during
582 their oxidation by sulpho-oxidizing bacteria. Moreover, theoretical calculations of Se^{2-} or
583 $\text{Se}(0)$ oxidation by NO_3^- and O_2 show favourable Gibbs free energies for their oxidation by
584 NO_3^- , indicating that NO_3^- can act as an electron acceptor for Se oxidation (Wright, 1999). As
585 the distance to the corridor increases according to the pumping-induced flow directions, the
586 general dynamic is a decrease of oxic conditions with less intense oxidation, resulting in very
587 low Se and NO_3^- concentrations.

588 Except for the redox sequence, NO_3^- concentrations above 10 mg L^{-1} in groundwater
589 (grey circles on Fig. 3) are associated with Se concentrations limited to $20 \mu\text{g L}^{-1}$, which is
590 defined as the maximum natural threshold value (Fig. 3). This reflects oxic conditions, where
591 pyrite is not usually present. The decrease of Se values from 20 to $<0.5 \mu\text{g L}^{-1}$ corresponds to
592 NO_3^- values from 10 mg L^{-1} to <0.5 , which means that NO_3^- and SeO_4^{2-} reduction can occur
593 simultaneously. This is coherent with bibliographic data from microbiological laboratory
594 experiments, with threshold values of $5\text{-}10 \text{ mg L}^{-1}$ of NO_3^- above which Se(VI) reduction is
595 inhibited (Tan et al., 2018; Thouin et al., 2019).

596 In view of the above, pyrite plays an important role. In the Louvil Clays, it contains 7
597 to 29% of the total Se stock, $48\text{-}61\%$ of the available stock already being associated with
598 pyritic compounds, meaning that most of the “bioavailable” Se is already trapped in these

599 reduced sulphur compounds. We do not know the Se content of pyrite contained in Chalk,
600 but we can assume that its potential as a Se-release source or for Se-trapping is important
601 and will grow with time. Indeed, the superimposition of multi-year alternations of oxidation
602 and reduction processes has generated a large and variously crystallized pool of pyrite in the
603 Chalk porosity controlled by water-level fluctuations in the Chalk aquifer.

604 **5.7 Short- and long-term contaminants cycles**

605 Considering relatively short cycles at a multi-annual scale, groundwater goes through
606 transient states according to recharge, mixing with waters from the fracture corridor, and
607 pumping. This suggests that Fe, Mn and associated trace metals S and Se, undergo multiple
608 cycles of oxidation, mobilization, and re-reduction, resulting in a metal-rich redox front.

609 For longer cycles, we can suppose that the redox front has been migrating downward
610 since emersion of the region, and that this migration is dependent on overall changes in
611 recharge and exploitation. In the main wells of the study area, the present-day dynamic level
612 reaches its lowest depth in the Chalk aquifer and moves ever closer down to the estimated
613 non-productive zone of the aquifer, after 50 years of large (± 20 m) variations in the water-
614 level depth. The base of the Louvil Clays therefore remains mainly unsaturated, today.

615 With -8% of precipitation and +4% of evapotranspiration since 2016 (MeteoFrance
616 data), relative to the 1981-2010 period (Picot and Bourguine, 2010), the local climate-change
617 effect is dominated by a sharp decrease in groundwater recharge (-7%), and over three to
618 four months instead of six, before. Although demand is growing, the official extraction rates
619 were decreased from 37 to 31 Mm³/year between 2016 and 2020, to preserve the well field
620 that has reached its maximum capacity. Under these conditions, the transfer of elements
621 from the primary Louvil Clays source probably has been notably reduced, especially for
622 metals, Se and organic matter, which may become a limiting factor for future redox reactions.

623 Only complete cessation of pumping would lead to a heightening of water levels,
624 creating the conditions for increasing water stocks in the Chalk. If we consider the imprints of
625 overall changes, evolution scenarios should be drawn for predicting Se speciation. Durable

626 exploitation of the well field should stabilize water-level fluctuations and the unsaturated
627 zone. The Se-in-Chalk stock would not increase, Se mobility would be driven by pyrite
628 formation and dissolution, and bacterial reduction processes would depend on geology
629 constraints. It would thus be interesting to assess the role of Se in pyrite-formation rate, as
630 trace elements such as Ni or As respectively accelerate or inhibit pyrite formation (Baya et
631 al., 2021). However, a large reduction in pumping or abandonment of the well field would
632 recreate the reductive conditions for lowering Se mobility, e.g., by stocking Se in the pyrite
633 pool of the Chalk, but would also increase Se(IV) concentrations until the conditions are
634 favourable for Se(0) formation. To better understand the effects of global climate change on
635 the biogeochemical cycling of redox-sensitive elements, a reactive transport model (Shultz et
636 al., 2018) could be used and coupled with the existing hydrogeological model for testing
637 various scenarios of groundwater use.

638 **6. Conclusions**

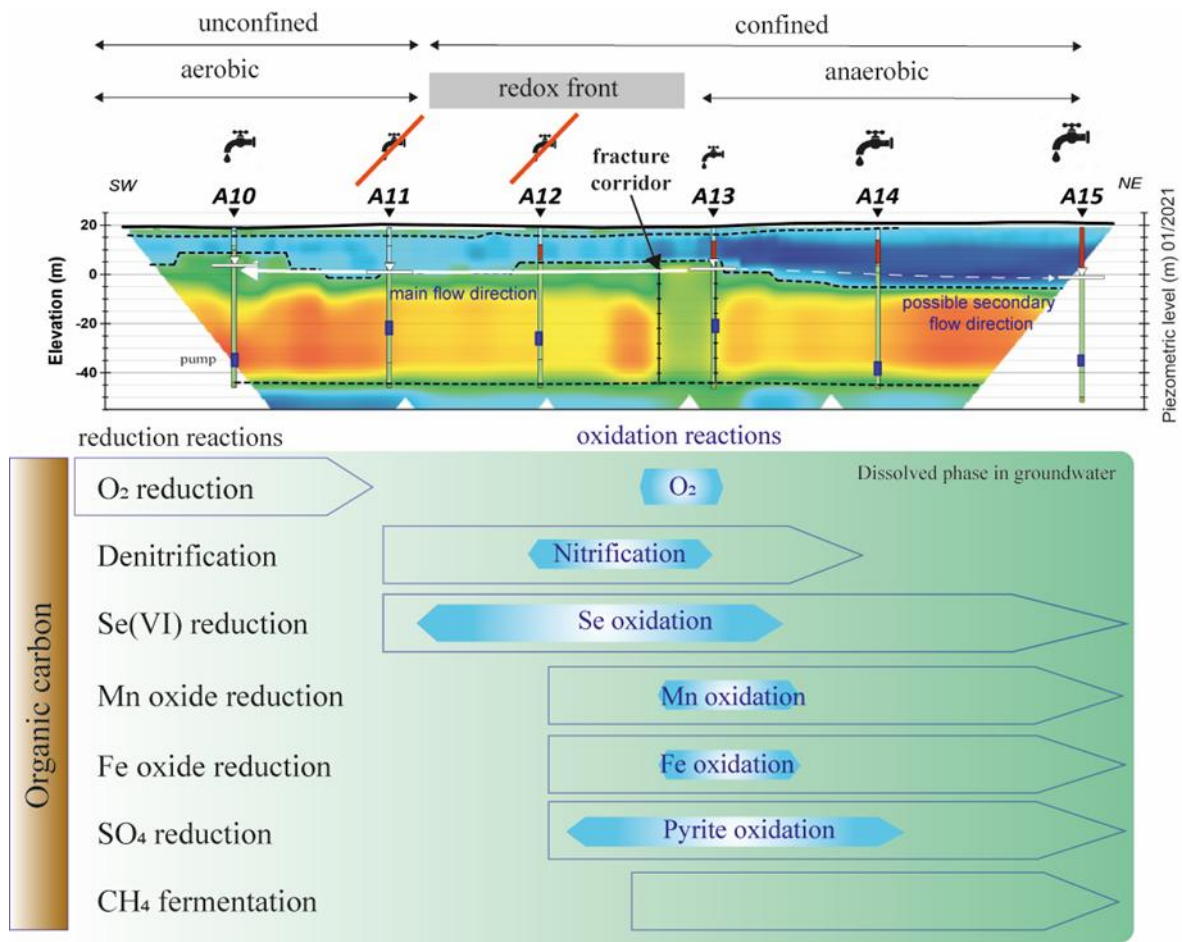
639
640 The selenium cycle is affected by processes of a redox sequence, potentially leading to high
641 Se concentrations in groundwater. The spatial and temporal disparities of Se concentrations
642 in a dynamic system, are controlled by geological and hydrogeological constraints—here the
643 presence of Se-enriched Louvil Clays that progressively confine the Chalk aquifer—and by
644 variations in the water-level depth induced by recharge and pumping. Our conceptual
645 scheme presents the main reductive processes in the Les Ansereuilles succession near Lille
646 (France), and the superimposition of localized oxidation processes, mainly pyrite oxidation,
647 on the investigated Critical Zone, resulting in a Se hot spot (Fig. 7). Here, the Se-rich redox
648 front has been steadily migrating downward in the water-level fluctuation zone of the Chalk
649 aquifer.

650 Over the past years, low recharge has not compensated groundwater exploitation and
651 the recent pandemic has further increased a growing water demand. However, the pool of Se
652 in the Chalk aquifer may not increase very much in the coming years, as the base of the

653 Louvil Clays, a Se source, will remain under unsaturated conditions. The key challenge
654 remains the mobility of the Se pool in the Chalk aquifer, linked with the presence of pyrite.
655 Concerning the other parts of the well fields, outside the redox sequence, Se mainly occurs
656 in Quaternary sediments, where the natural background concentration range is 10-20 $\mu\text{g L}^{-1}$.
657 Increased precipitation or flooding is expected to lead to a potential change in soil redox
658 conditions, coupled with rapid input of oxygen, and possibly nitrates, into the system, as well
659 as a major impact on biogeochemical processes and Se mobility.

660 Key parameters for evaluating Se mobility under global change, are changes in nitrate
661 concentrations in groundwater and in bacterial activity in the water-level fluctuation zone.
662 Most of the well fields being in agricultural land, the challenge is to develop strategies for
663 limiting nitrate entries to improve groundwater quality. However, Se distribution and
664 speciation, which are controlled by redox reactions and biogeochemical processes, must first
665 be better assessed through considering the complete Se biogeochemical cycle, including
666 solid and organic Se forms. To fully unravel the reactivity and transfer of Se, Se isotopes
667 should be useful indicators.

668



669

670 *Figure 7: Lateral evolution of reductive reactions along the A10-A15 transect and local superimposition*
 671 *of oxidation reactions. The taps symbolize groundwater pumping rates and well closure due to high Se*
 672 *contents (A12 and A11). The geophysical profile shows resistivity variations, from low (blue) to high*
 673 *(red), and illustrates the progressive confinement of the Chalk aquifer by the Louvil Clays (in deep*
 674 *blue). The Chalk is divided in green (productive) and orange (less productive) parts where the pumps*
 675 *are now located. The main flow direction is indicated (wells A13 to A10), and also a possible*
 676 *secondary one (A13-A15) that may vary with pumping intensity. The large arrows symbolize reductive*
 677 *reactions that are laterally staggered with oxidation processes. The fracture corridor near well A13*
 678 *supplies oxygenated groundwater to the reductive system by mixing, that superimposes local oxidation*
 679 *reactions symbolized by the blue double arrows. The reaction domains are drawn at well scale (about*
 680 *200 m spacing). Organic carbon provides electrons to the reduction reactions.*

681

682 **Acknowledgments**

683 This study was supported financially and technically by the Lille European Metropolis, the
 684 French Geological Survey (BRGM), Eaux du Nord, Noréade, the University of Lille, and the
 685 Artois-Picardie Water Agency, in the context of projects COHMET (2017-2020), Thermosel
 686 (2011-2013) and Geo2020 (2020-2021). The authors thank M. Walaszek (LASIRE-BRGM),

687 F. Joublin and G. Bentivegna (BRGM), E. Bugner (MEL laboratory) and P. Daudruy
688 (SOURCEO) for their technical and scientific support during sampling and water analyses.
689 The work benefited from the collaboration of C. Guerrot, C. Fléhoc and A.M. Gallas (BRGM
690 Mass-Spectrometry team) who provided the $\delta^{34}\text{S}_{\text{SO}_4}$ and $\delta^{18}\text{O}_{\text{SO}_4}$ isotopic analyses, and of T.
691 Conte (BRGM Chemistry laboratories) who provided the major- and trace-element analyses.
692 Several ICP-AES and ICP-MS measurements were also performed on the Chevreul Institute
693 Platform (U-Lille/CNRS). The Region Hauts de France and the French government are
694 acknowledged for co-funding of these apparatus. We thank the landowner of the fields
695 crossed by the geophysical profile. H.M. Kluijver edited the final English manuscript for
696 language and content. The authors are grateful to the Editor and the two anonymous
697 reviewers for thoughtful revisions of the manuscript and constructive comments.

698

699 **References**

- 700 Acworth, R., 1987. The development of crystalline basement aquifers in a tropical
701 environment. *Quarterly Journal of Engineering Geology and Hydrogeology*, 20(4),
702 20(4): 265-272.
- 703 ADEME, 2007. Bilan des flux de contaminants entrant sur les sols agricoles de France
704 métropolitaine. Bilan qualitatif de la contamination par les éléments tracés
705 métalliques et les composés tracés organiques et application quantitative pour les
706 éléments traces métalliques. SOGREAH. 329 p.
- 707 Ashok, V., Subrata, H., 2015. Remediation of Nitrate-Contaminated Water by Solid-Phase
708 Denitrification Process-a Review. *Environmental Science and Pollution Research*,
709 22(11).
- 710 Bailey, R.T., 2016. Review: Selenium contamination, fate, and reactive transport in
711 groundwater in relation to human health. *Hydrogeology Journal*: 1-27.
- 712 Bailey, R.T., Hunter, W.J., Gates, T.K., 2012. The Influence of Nitrate on Selenium in
713 Irrigated Agricultural Groundwater Systems. *Journal of Environmental Quality*, 41(3):
714 783-792.
- 715 Baize, D., Douay, F., Villanneau, E., Bourennane, H., Sterckeman, T., Ciesielski, H., King,
716 D., 2010. Les éléments en traces dans les sols agricoles du Nord-Pas-de-Calais, I.
717 Étude et cartographie des teneurs des horizons de surface. *Etude et Gestion des*
718 *Sols*, 17: 213-237.
- 719 Bajaj, M., Eiche, E., Neumann, T., Winter, J., Gallert, C., 2011. Hazardous concentrations of
720 selenium in soil and groundwater in North-West India. *Journal of Hazardous*
721 *Materials*, 189: 640-6.
- 722 Barron, E., Migeot, V., Rabouan, S., Potin-Gautier, M., Seby, F., Hartemann, P., Levi, Y.,
723 Legube, B., 2009. The case for re-evaluating the upper limit value for selenium in
724 drinking water in Europe. *Journal of Water and Health*, 7(4): 630-641.

- 725 Baya, C., Le Pape, P., Baptiste, B., Brest, J., Landrot, G., Elkaim, E., Noël, V., Blanchard,
726 M., Ona-Nguema, G., Juillot, F., Morin, G., 2021. Influence of trace level As or Ni on
727 pyrite formation kinetics at low temperature. *Geochimica et Cosmochimica Acta*, 300:
728 333-353.
- 729 Beisner, K., Naftz, D.L., Johnson, W.P., Diaz, X., 2009. Selenium and trace element mobility
730 affected by periodic displacement of stratification in the Great Salt Lake, Utah.
731 *STOTEN*, 407(19): 5263-5273.
- 732 Belle, P., Lachassagne, P., Mathieu, F., Barbet, C., Brisset, N., Gourry, J.-C., 2019.
733 Characterization and location of the laminated layer within hard rock weathering
734 profiles from electrical resistivity tomography: implications for water well siting.
735 *Geological Society, London*, 479(1): 187-205.
- 736 Bernard, D., 1979. Contribution à l'étude hydrogéochimique de la nappe de la craie dans le
737 nord de la France. BRGM/79-SGN-245-NPC, Université des sciences et techniques
738 de Lille, Lille.
- 739 Bernard, D., Bosch, B., Caulier, P., 1981. Acquisition et rassemblement des données
740 géothermiques disponibles et nouvelles dans la zone Franco-Belge de Saint-Ghislain
741 à Saint-Amand-les-Eaux (Nord).
- 742 Bessière, H., Picot, J., Picot, G., Parmentier, M., 2015. Affinement du modèle
743 hydrogéologique de la craie du Nord-Pas-de-Calais autour des champs captants de
744 la métropole lilloise. BRGM/RP-63689-FR.
- 745 Borch, T., Kretzschmar, R., Kappler, A., Cappellen, P.V., Ginder-Vogel, M., Voegelin, A.,
746 Campbell, K., 2010. Biogeochemical Redox Processes and their Impact on
747 Contaminant Dynamics. *Environmental Science & Technology*, 44(1): 15-23.
- 748 Brenot, A., Baran, N., Petelet-Giraud, E., Négrel, P., 2008. Interaction between different
749 water bodies in a small catchment in the Paris basin (Brévilles, France): Tracing of
750 multiple Sr sources through Sr isotopes coupled with Mg/Sr and Ca/Sr ratios. *Applied
751 Geochemistry*, 23(1): 58-75.
- 752 Breynaert, E.C., Bruggeman, C., Maes, A., 2008. XANES-EXAFS analysis of Se solid-phase
753 reaction products formed upon contacting Se(IV) with FeS₂ and FeS *Environ. Sci.
754 Technol.*, 42: 3585-3601.
- 755 Brozmanová, J., Mániková, D., Vlčková, V., Chovanec, M., 2010. Selenium: a double-edged
756 sword for defense and offence in cancer. *Archives of Toxicology*, 84(12): 919-938.
- 757 Cary, L., Benabderraziq, H., Elkhatabi, J., Gourcy, L., Parmentier, M., Picot, J., Khaska, M.,
758 Laurent, A., Négrel, P., 2014. Tracking selenium in the Chalk aquifer of northern
759 France: Sr isotope constraints. *Applied Geochemistry*, 48(0): 70-82.
- 760 Chasteen, T.G., Bentley, R., 2003. Biomethylation of selenium and tellurium: Microorganisms
761 and plants. *Chemical Reviews*, 103(1): 1-25.
- 762 Comte, J.-C., Cassidy, R., Nitsche, J., Ofterdinger, U., Pilatova, K., Flynn, R., 2012. The
763 typology of Irish hard-rock aquifers based on an integrated hydrogeological and
764 geophysical approach. *Hydrogeology Journal*, 20(8): 1569-1588.

- 765 Coppin, F., Chabroulet, C., Martin-Garin, A., 2009. Selenite interactions with some
766 particulate organic and mineral fractions isolated from a natural grassland soil.
767 *European Journal of Soil Science*, 60(3): 369-376.
- 768 Darcheville, O., Février, L., Haichar, F.Z., Berge, O., Martin-Garin, A., Renault, P., 2008.
769 Aqueous, solid and gaseous partitioning of selenium in an oxic sandy soil under
770 different microbiological states. *Journal of Environmental Radioactivity*, 99(6): 981-
771 992.
- 772 De Temmerman, L., Waegeneers, N., Thiry, C., Du Laing, G., Tack, F., Ruttens, A., 2014.
773 Selenium content of Belgian cultivated soils and its uptake by field crops and
774 vegetables. *Science of The Total Environment*, 468–469(0): 77-82.
- 775 Descloitres, M., Ruiz, L., Sekhar, M., Legchenko, A., Braun, J.-J., Mohan Kumar, M.S.,
776 Subramanian, S., 2008. Characterization of seasonal local recharge using electrical
777 resistivity tomography and magnetic resonance sounding. *Hydrological Processes*,
778 22(3): 384-394.
- 779 Desoignies, J., Sangnier, P., 1968. Notice de la carte géologique de la France au 1/50 000
780 de Carvin (n°20) et de Lille (n°14). BRGM Ed.
- 781 Detmers, J., Brüchert, V., Habicht, K.S., Kuever, J., 2001. Diversity of sulfur isotope
782 fractionations by sulfate-reducing prokaryotes. *Applied and Environmental*
783 *Microbiology*, 67(2): 888-894.
- 784 Dhillon, K.S., Dhillon, S.K., 1991. Selenium toxicity in soils, plants and animals in some parts
785 of Punjab, India. *International Journal of Environmental Studies*, 37(1-2): 15-24.
- 786 Dhillon, K.S., Dhillon, S.K., 2014. Development and mapping of seleniferous soils in
787 northwestern India. *Chemosphere*, 0.
- 788 Diehl, S.F., Goldhaber, M.B., Koenig, A.E., Lowers, H.A., Ruppert, L.F., 2012. Distribution of
789 arsenic, selenium, and other trace elements in high pyrite Appalachian coals:
790 Evidence for multiple episodes of pyrite formation. *International Journal of Coal*
791 *Geology*, 94(0): 238-249.
- 792 Dowdle, P.R., Oremland, R.S., 1998. Microbial oxidation of elemental selenium in soil
793 slurries and bacterial cultures. *Environ. Sci. Technol.*, 32: 3749-3755.
- 794 Edmunds, W.M., Cook, J.M., Darling, W.G., Kinniburgh, D.G., Miles, D.L., Bath, A.H.,
795 Morgan-Jones, M., Andrews, J.N., 1987. Baseline geochemical conditions in the
796 Chalk aquifer, Berkshire, UK: a basis for groundwater quality management. *Applied*
797 *Geochemistry*, 2(3): 251-274.
- 798 Edmunds, W.M., Shand, P., Hart, P., Ward, R.S., 2003. The natural (baseline) quality of
799 groundwater: a UK pilot study. *Science of The Total Environment*, 310(1-3): 25-35.
- 800 Fernández-Martínez, A., Charlet, L., 2009. Selenium environmental cycling and
801 bioavailability: a structural chemist point of view. *Reviews in Environmental Science*
802 *and Bio/Technology*, 8(1): 81-110.
- 803 Gates, T.K., Cody, B.M., Donnelly, J.P., Herting, A.W., Bailey, R.T., Price, J.M., 2009.
804 Assessing Selenium Contamination in the Irrigated Stream-Aquifer System of the
805 Arkansas River, Colorado. *Journal of Environmental Quality*, 38(6): 2344-2356.

- 806 Goldberg, S., Lesch, S.M., Suarez, D.L., 2007. Predicting selenite adsorption by soils using
807 soil chemical parameters in the constant capacitance model. *Geochimica et*
808 *Cosmochimica Acta*, 71(23): 5750-5762.
- 809 Gourcy, L., Crastes de Paulet, F., Laurent, A., 2013. Sulfur origin and influences of water
810 level variation on SO₄ concentration in groundwater of the transboundary
811 Carboniferous Limestone Aquifer (Belgium, France). *Procedia Earth and Planetary*
812 *Science*, 7(0): 309-312.
- 813 Gourcy, L., Lions, J., Wyns, R., Dictor, M., Brenot, A., Crouzet, C., Ghestem, J., 2011.
814 Origine du sélénium et compréhension des processus dans les eaux du bassin
815 Seine-Normandie. Rapport final. BRGM/RP-59445-FR, 178 p.
- 816 Herbel, M.J., Blum, J.S., Oremland, R.S., Borglin, S.E., 2003. Reduction of Elemental
817 Selenium to Selenide: Experiments with Anoxic Sediments and Bacteria that Breathe
818 Se-Oxyanions. *Geomicrobiology Journal*, 20(6): 587-602.
- 819 Huerta-Diaz, M.A., Morse, J.W., 1990. A quantitative method for determination of trace metal
820 concentrations in sedimentary pyrite. *Marine Chemistry*, 29: 119-144.
- 821 Huggett, J.M., Knox, R.W.O.B., 2006. Clay mineralogy of the Tertiary onshore and offshore
822 strata of the British Isles. *Clay Minerals*, 41(1): 5-46.
- 823 Kang, M., Bardelli, F., Ma, B., Charlet, L., Chen, F., Yang, Y., 2016. The influence of pH and
824 reaction time on the formation of FeSe₂ upon selenite reduction by nano-sized pyrite-
825 greigite. *Radiochimica Acta*, 104(9): 649-656.
- 826 Kang, M., Chen, F., Wu, S., Yang, Y., Bruggeman, C., Charlet, L., 2011. Effect of pH on
827 Aqueous Se(IV) Reduction by Pyrite. *Environmental Science & Technology*, 45(7):
828 2704-2710.
- 829 Kappler, A., Straub, K.L., 2005. Geomicrobiological Cycling of Iron. *Reviews in Mineralogy*
830 *and Geochemistry*, 59(1): 85-108.
- 831 Kloppmann, W., Dever, L., Edmunds, W.M., 1998. Residence time of Chalk groundwaters in
832 the Paris Basin and the North German Basin: a geochemical approach. *Applied*
833 *Geochemistry*, 13(5): 593-606.
- 834 Kulp, T.R., Pratt, L.M., 2004. Speciation and weathering of selenium in upper Cretaceous
835 chalk and shale from South Dakota and Wyoming, USA. *Geochimica Cosmochimica*
836 *Acta*, 68(18): 3687-3701.
- 837 Liu, X., Fattahi, M., Montavon, G., Grambow, B., 2008. Selenide retention onto pyrite under
838 reducing conditions. *Radiochimica Acta*, 96(8): 473-479.
- 839 Liu, Y.T., Chen, T.Y., Mackebee, W.G., Ruhl, L., Vengosh, A., Hsu-Kim, H., 2013. Selenium
840 speciation in coal ash spilled at the Tennessee Valley Authority Kingston Site.
841 *Environmental Science & Technology*, 47(24): 14001-14009.
- 842 Loke, M.H., 2015. Tutorial: 2-D and 3-D electrical imaging surveys. *Geotomo Softw.*
843 *Malaysia* 127.
- 844 Loke, M.H., 2020. RES2DINVx64 ver. 4.10. *Geotomo Softw.* SDN BHD - Aarhus
845 *GeoSoftware*.

- 846 Mariotti, A., Landreau, A., Simon, B., 1988. ^{15}N isotope biogeochemistry and natural
847 denitrification process in groundwater: Application to the chalk aquifer of northern
848 France. *Geochimica et Cosmochimica Acta*, 52(7): 1869-1878.
- 849 Masscheleyn, P.H., Delaune, R.D., Patrick, W.H., 1991. Biogeochemical behavior of
850 selenium in anoxic soils and sediments: An equilibrium thermodynamics approach.
851 *Journal of Environmental Science and Health . Part A: Environmental Science and*
852 *Engineering and Toxicology*, 26(4): 555-573.
- 853 Mast, M.A., Mills, T.J., Paschke, S.S., Keith, G., Linard, J.I., 2014. Mobilization of selenium
854 from the Mancos Shale and associated soils in the lower Uncompahgre River Basin,
855 Colorado. *Applied Geochemistry*, 48: 16-27.
- 856 Meire, B., Portal, A., Jacob, T., Paquet, F., Bitri, A., Mathieu, F., David, P.-Y., 2019.
857 Fonctionnement de l'hydro-système, interactions et cheminements des eaux
858 naturelles et de la n-nitrosomorpholine dans le secteur de la Faille de Lillebonne -
859 Fécamp (76) - Volet géologique et géophysique. Rapport final. BRGM/RP-67087-FR.
- 860 Mitchell, K., Couture, R.-M., Johnson, T.M., Mason, P.R.D., Van Cappellen, P., 2013.
861 Selenium sorption and isotope fractionation: Iron(III) oxides versus iron(II) sulfides.
862 *Chemical Geology*, 342(0): 21-28.
- 863 Mitchell, K., Mason, P.R.D., Van Cappellen, P., Johnson, T.M., Gill, B.C., Owens, J.D., Diaz,
864 J., Ingall, E.D., Reichart, G.-J., Lyons, T.W., 2012. Selenium as paleo-oceanographic
865 proxy: A first assessment. *Geochimica et Cosmochimica Acta*, 89: 302-317.
- 866 Naveau, A., Monteil-Rivera, F., Guillon, E., Dumonceau, J., 2007. Interactions of aqueous
867 selenium (-II) and (IV) with metallic sulfide surfaces. *Environmental Science &*
868 *Technology*, 41(15): 5376-5382.
- 869 Neal, R.H., Sposito, G., 1989. Selenate Adsorption on Alluvial Soils. *Soil Science Society of*
870 *America Journal*, 53(1): 70-74.
- 871 Négrel, P., Petelet-Giraud, E., 2005. Strontium isotopes as tracers of groundwater-induced
872 floods: the Somme case study (France). *Journal of Hydrology*, 305(1-4): 99-119.
- 873 Nkansah-Boadu, F., 2019. Removal of Soluble Selenium in the Presence of Nitrate from
874 Coal Mining-Influenced Water.
- 875 Ohlendorf, H.M., Santolo, G.M., 1994. Kesterson reservoir. Past, present, and future: An
876 ecological risk assessment. In: Frankenberger, W.T., Benson, S. (Eds.), *Selenium in*
877 *the environment*. Dekker, Marcel., New York, pp. 69-117.
- 878 Oremland, R.S., Blum, J.S., Bindi, A.B., Dowdle, P.R., Herbel, M., Stolz, J.F., 1999.
879 Simultaneous reduction of nitrate and selenate by cell suspensions of selenium-
880 respiring bacteria. *Applied and Environmental Microbiology*, 65(10): 4385-4392.
- 881 Oremland, R.S., Hollibaugh, J.T., Maest, A.S., Presser, T.S., Miller, L.G., Culbertson, C.W.,
882 1989. Selenate reduction to elemental selenium by anaerobic bacteria in sediments
883 and culture: biogeochemical significance of a novel, sulfate-independent respiration.
884 *Appl Environ Microbiol*, 55(9): 2333-2343.
- 885 Parmentier, M., Ollivier, P., Joulian, C., Albrecht, A., Hadi, J., Greneche, J.-M., Pauwels, H.,
886 2014. Enhanced heterotrophic denitrification in clay media: The role of mineral
887 electron donors. *Chemical Geology*, 390: 87-99.

- 888 Parnell, J., Brolly, C., Spinks, S., Bowden, S., 2016. Selenium enrichment in Carboniferous
889 Shales, Britain and Ireland: Problem or opportunity for shale gas extraction? Applied
890 Geochemistry, 66: 82-87.
- 891 Peters, G.M., Maher, W.A., Barford, J.P., Gomes, V.G., 1997. Selenium Associations in
892 Estuarine Sediments: Redox Effects. In: Evans, R.D., Wisniewski, J., Wisniewski, J.R.
893 (Eds.), The Interactions Between Sediments and Water: Proceedings of the 7th
894 International Symposium, Baveno, Italy 22–25 September 1996. Springer
895 Netherlands, Dordrecht, pp. 275-282.
- 896 Picot, J., Bourguin, B., 2010. Modélisation géologique de la craie céno-turonienne en région
897 Nord-Pas-de-Calais. Rapport final.
- 898 Portal, A., Jacob, T., Meire, B., Bretaudeau, F., Mathieu, F., Paquet, F., David, P.-Y., 2020.
899 Modèle mathématique de gestion de l'hydro-système Seine - craie - alluvions sur les
900 territoires de la Métropole de Rouen Normandie et du syndicat mixte du SAGE Cailly-
901 Aubette-Robec. Rapport n°2 : Résultats des investigations géophysiques. Rapport
902 final.
- 903 Rayman, M.P., 2000. The importance of selenium to human health. *Lancet* 356: 233-241.
- 904 Revil, A., Karaoulis, M., Johnson, T., Kemna, A., 2012. Review: Some low-frequency
905 electrical methods for subsurface characterization and monitoring in hydrogeology.
906 *Hydrogeology Journal*, 20: 617-658.
- 907 Ryser, A.L., Strawn, D.G., Marcus, M.A., Johnson-Maynard, J.L., Gunter, M.E., Möller, G.,
908 2005. Micro-spectroscopic investigation of selenium-bearing minerals from the
909 Western US Phosphate Resource Area. *Geochemical transactions*, 6(1): 1-1.
- 910 Schellenger, A.E., Larese-Casanova, P., 2013. Oxygen isotope indicators of selenate
911 reaction with Fe(II) and Fe(III) hydroxides. *Environ Sci Technol*, 47(12): 6254-62.
- 912 Séby, F., Potin Gautier, M., Lespés, G., Astruc, M., 1997. Selenium speciation in soils after
913 alkaline extraction. *Science of The Total Environment*, 207(2–3): 81-90.
- 914 Sharma, V., McDonald, T., Sohn, M., Anquandah, G., Maurizio, P., Zboril, R., 2014.
915 Biogeochemistry of selenium. A review. *Environmental Chemistry Letters*, 13: 49-58.
- 916 Shultz, C.D., Gates, T.K., Bailey, R.T., 2018. Evaluating best management practices to lower
917 selenium and nitrate in groundwater and streams in an irrigated river valley using a
918 calibrated fate and reactive transport model. *Journal of Hydrology*, 566: 299-312.
- 919 Simon, B., 1986. Apports de la biogéochimie isotopique à la connaissance de la
920 dénitrification dans les eaux souterraines. 86-SGN-641
- 921 Stillings, L.L., Amacher, M.C., 2010. Kinetics of selenium release in mine waste from the
922 Meade Peak Phosphatic Shale, Phosphoria Formation, Wooley Valley, Idaho, USA.
923 *Chemical Geology*, 269(1–2): 113-123.
- 924 Stumm, W., Morgan, J.J., 1996. Precipitation and dissolution. In: (Eds), J.W.S. (Ed.), *Aquatic
925 chemistry. Chemical Equilibria and Rates in Natural Waters*, New York, pp. 329-424.
- 926 Tan, L.C., Nancharaiah, Y.V., van Hullebusch, E.D., Lens, P.N.L., 2018. Effect of elevated
927 nitrate and sulfate concentrations on selenate removal by mesophilic anaerobic

- 928 granular sludge bed reactors. *Environmental Science-Water Research & Technology*,
929 4(2): 303-314.
- 930 Thode, H.G., 1991. Sulphur isotopes in nature and the environment: an overview. In:
931 H.R.Krouse and V.A. Grinenko (Ed.) *Stable isotopes : Natural and anthropogenic*
932 *sulphur in the Environmental*. SCOPE 43, J.Wiley and Sons, Chichester, pp.1-26.
- 933 Thouin, H., Cary, L., Charron, M., Joulian, C., Klinka, T., Battaglia-Brunet, F., 2019.
934 Occurrence of arsenic and selenium in aquifers used to produce drinking water near
935 Orleans, France: indices of active biogeochemical processes, 24th International
936 Symposium on Environmental Biogeochemistry, Potsdam, Germany.
- 937 Tugarova, A.V., Vetchinkina, E.P., Loshchinina, E.A., Shchelochkov, A.G., Nikitina, V.E.,
938 Kamnev, A.A., 2013. The ability of the rhizobacterium *Azospirillum brasilense* to
939 reduce selenium(IV) to selenium(0). *Microbiology*, 82(3): 352-355.
- 940 Tuttle, M.L.W., Fahy, J.W., Elliott, J.G., Grauch, R.I., Stillings, L.L., 2014. Contaminants from
941 Cretaceous black shale: II. Effect of geology, weathering, climate, and land use on
942 salinity and selenium cycling, Mancos Shale landscapes, southwestern United States.
943 *Applied Geochemistry*.
- 944 Van Stempvoort, D.R., Hendry, M.J., Schoenau, J.J., Krouse, H.R., 1994. Sources and
945 dynamics of sulfur in weathered till, Western Glaciated Plains of North America.
946 *Chemical Geology*, 111(1): 35-56.
- 947 Vinceti, M., Crespi, C.M., Bonvicini, F., Malagoli, C., Ferrante, M., Marmiroli, S., Stranges, S.,
948 2013. The need for a reassessment of the safe upper limit of selenium in drinking
949 water. *STOTEN*, 443: 633-642.
- 950 Vitòria, L., Soler, A., Canals, À., Otero, N., 2008. Environmental isotopes (N, S, C, O, D) to
951 determine natural attenuation processes in nitrate contaminated waters: Example of
952 Osona (NE Spain). *Applied Geochemistry*, 23(12): 3597-3611.
- 953 Walaszek, M., Cary, L., Billon, G., Blessing, M., Bouvet-Swialkowski, A., George, M., Criquet,
954 J., Mossmann, J.R., 2021. Dynamics of chlorinated aliphatic hydrocarbons in the
955 Chalk aquifer of northern France. *Science of The Total Environment*, 757: 143742.
- 956 Wright, W.G., 1999. Oxidation and mobilization of selenium by nitrate in irrigation drainage.
957 *Journal of Environmental Quality*, 28(4): 1182-1187.
- 958 Xu, W., Zhu, J.-M., Johnson, T.M., Wang, X., Lin, Z.-Q., Tan, D., Qin, H., 2020. Selenium
959 isotope fractionation during adsorption by Fe, Mn and Al oxides. *Geochimica et*
960 *Cosmochimica Acta*, 272: 121-136.
- 961 Yang, G.Q., Wang, S.Z., Zhou, R.H., Sun, S.Z., 1983. Endemic selenium intoxication of
962 humans in China. *Am J Clin Nutr*, 37: 872-881.
- 963 Zhang, Y.-C., Slomp, C.P., Broers, H.P., Bostick, B., Passier, H.F., Böttcher, M.E.,
964 Omeregie, E.O., Lloyd, J.R., Polya, D.A., Van Cappellen, P., 2012. Isotopic and
965 microbiological signatures of pyrite-driven denitrification in a sandy aquifer. *Chemical*
966 *Geology*, 300–301(0): 123-132.
- 967 Zhang, Y.Q., Moore, J.N., 1996. Selenium fractionation and speciation in a wetland system.
968 *Environmental Science & Technology*, 30(8): 2613-2619.

969

970